















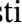





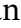





# GRB 210704A: a luminous fast blue transient in a GRB afterglow at $z=2.34$

Daniëlle L. A. Pieterse <sup>1</sup>★, Andrew J. Levan <sup>1,2</sup>, Maria E. Ravasio <sup>1,3</sup>, Jillian C. Rastinejad <sup>4,5</sup>,  
 Agnes P. C. van Hoof <sup>1</sup>, Daniele B. Malesani <sup>1,6,7</sup>, Nikhil Sarin <sup>8,9</sup>, Gavin P. Lamb <sup>10</sup>,  
 Antonio Martin-Carrillo <sup>11</sup>, Anya E. Nugent <sup>12</sup>, Nial R. Tanvir <sup>13</sup>, Peter G. Jonker <sup>1</sup>,  
 David Alexander Kann <sup>14,15</sup>†, José Feliciano Agüí Fernández <sup>16</sup>, Edo Berger <sup>12</sup>,  
 Gregory Corcoran <sup>11</sup>, Felice Cusano <sup>17</sup>, Paolo D’Avanzo <sup>3</sup>, Valerio D’Elia <sup>18</sup>,  
 Antonio de Ugarte Postigo <sup>19</sup>, Dimple <sup>20,21</sup>, Wen-fai Fong <sup>4</sup>, Johan P.U. Fynbo <sup>6,7</sup>,  
 Luca Izzo <sup>22,23</sup>, Elisabetta Maiorano <sup>17</sup>, Andrea Melandri <sup>24</sup>, Eliana Palazzi <sup>17</sup>,  
 Jonathan Quirola-Vásquez <sup>1</sup>, Andrea Rossi <sup>17</sup> and Alicia Rouco Escorial <sup>25</sup>

*Affiliations are listed at the end of the paper*

Accepted 2026 March 18. Received 2026 March 18; in original form 2025 December 8

## ABSTRACT

We present detailed multiwavelength analysis of GRB 210704A: a *Fermi* Gamma-ray Burst Monitor discovered and *Fermi* Large Area Telescope (LAT) detected gamma-ray burst (GRB). The burst is dominated by a short ( $\approx 2$  s) pulse followed by weaker softer emission. We line stack our afterglow spectrum and determine the most likely redshift to be  $z = 2.34$ . This is corroborated by the photometric redshift of the extended source underlying the GRB. The spectral energy distribution fit parameters, late-time imaging, as well as the GRB’s energetics, spectral lag, and location point to a collapsar nature. Follow-up observations reveal excess optical/infrared emission with respect to a standard afterglow, peaking around  $T_0 + 7$  d (2 d in the rest frame). The excess is extremely luminous ( $M_r = -22.0$  mag) and rapidly evolving. Strikingly, it resembles the emission seen in recently discovered *Einstein Probe* fast X-ray transients EP241021a and EP240414a, as well as the population of luminous fast blue optical transients (LFBOTs). This provides a link between these sources and GRBs. *Fermi*/LAT observations imply a high Lorentz factor, making this a case where LFBOT-like emission is also associated with a powerful successfully launched jet. We model the excess as likely coming from an energetic refreshed shock.

**Key words:** gamma-ray burst: general – gamma-ray burst: individual: GRB 210704A – supernovae: general – gamma-ray bursts – transients: supernovae.

## 1 INTRODUCTION

Gamma-ray bursts (GRBs) are the most energetic explosions in the Universe. GRBs are categorized into two classes based on their prompt emission duration (J. P. Norris et al. 1984; C. Kouveliotou et al. 1993): long GRBs (LGRBs;  $T_{90} > 2$  s) and short GRBs (SGRBs). Here  $T_{90}$  is the duration in which 5–95 per cent of the burst fluence is observed. Although this division is empirical, it is often employed to reflect a physical distinction in progenitor systems. LGRBs are commonly associated with the core-collapse of massive stars. This is evidenced by accompanying broad-lined Type Ic supernovae (SNe Ic-BL; e.g. T. J. Galama et al. 1998; J. Hjorth et al. 2003) and associations to star-forming, low-mass, and low-metallicity galaxies (A. S. Fruchter et al. 2006; D. A.

Perley et al. 2013; J. T. Palmerio et al. 2019). In contrast, SGRBs are typically attributed to compact object mergers involving neutron stars, where the radioactive decay of neutron-rich ejecta powers a kilonova (e.g. N. R. Tanvir et al. 2013; B. P. Abbott et al. 2017; A. Goldstein et al. 2017; B. D. Metzger 2019). SGRBs are connected to a variety of host galaxies, including quiescent hosts, and can be found at larger offsets due to natal kicks and in more massive hosts with a broader range of metallicities (A. Levan et al. 2016; W.-f. Fong et al. 2022; A. E. Nugent et al. 2022; B. O’Connor et al. 2022).

This classification scheme is enriched by the subclass of SGRBs with extended emission (EE-GRBs; J. P. Norris & J. T. Bonnell 2006). In these bursts, the initial short hard gamma-ray spike is followed by longer lasting, softer emission (e.g. Y. Kaneko et al. 2015). EE-GRBs are typically associated with compact object mergers (B. P. Gompertz, A. J. Levan & N. R. Tanvir 2020), just like the SGRBs without extended emission. They also have host galaxies that are indistinguishable from the population of other SGRB

\* E-mail: [d.pieterse@astro.ru.nl](mailto:d.pieterse@astro.ru.nl)

† Deceased

hosts (W.-f. Fong et al. 2022). The physical origin of the extended emission remains debated. Proposed explanations include magnetar spin-down (B. D. Metzger, E. Quataert & T. A. Thompson 2008; N. Bucciantini et al. 2012), fallback accretion (S. Rosswog 2007; B. D. Metzger et al. 2010), multiple jet components (M. V. Barkov & A. S. Pozanenko 2011), and magnetic reconnection in the relativistic GRB jet (B. Zhang & H. Yan 2011).

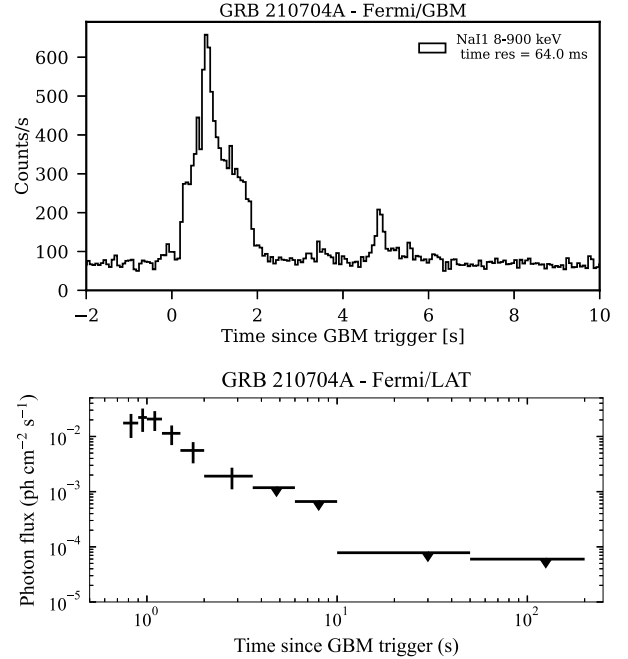
Recent discoveries have challenged the paradigm that LGRBs are created in collapsars and SGRBs in mergers. GRB 200826A (T. Ahumada et al. 2021; A. Rossi et al. 2022) was a short burst that was accompanied by an SN, revealing a collapsar nature. More markedly, LGRBs 211211A (J. C. Rastinejad et al. 2022; E. Troja et al. 2022; J. Yang et al. 2022) and 230307A (A. J. Levan et al. 2024; Y.-H. Yang et al. 2024) displayed compelling kilonova signatures, strongly suggesting compact object merger origins. Several more archival events can subsequently be added to this sample, including LGRBs 060614 (N. Gehrels et al. 2006; Z.-P. Jin et al. 2015; B. Yang et al. 2015) and 191019A (A. J. Levan et al. 2023; G. Stratta et al. 2025). These cases demonstrate that both LGRBs and SGRBs can emerge from diverse progenitors and that there is overlap between their formation channels.

GRB 210704A was a GRB with a short initial spike, followed by softer extended emission up to about 6 s (R. L. Becerra et al. 2023). It generated considerable interest within the astronomical community due to its borderline duration and possible EE-GRB classification, its high-energy GeV gamma-ray detections (A. Berretta et al. 2021), and its location in an apparent overdensity of luminous galaxies. The latter is of interest as these galaxies form plausible host galaxies for compact object merger progenitors (A. J. Levan et al. 2021). Follow-up observations revealed luminous optical/infrared (IR) excess emission with respect to a standard afterglow 5 d after the burst, prompting further questions about GRB 210704A’s physical origin.

Typically, the interaction of the GRB jet with the circumstellar medium (CSM) results in afterglow emission that decays as a power law with a slope of  $\alpha \approx -1.2$  (B. Zhang et al. 2006). Re-brightening phases have been observed hours to days after GRB explosions. They can be caused by e.g. the emergence of thermal transients such as SNe or kilonovae, non-uniform jet structures viewed off-axis, density variations in the CSM (X. Wang & A. Loeb 2000; Z. G. Dai & T. Lu 2002; D. Lazzati et al. 2002; E. Nakar, T. Piran & J. Granot 2003), SN–CSM interaction (e.g. M. Fraser 2020; B. Margalit 2022), or prolonged central-engine activity. The latter includes refreshed shocks, where the central engine ejects shells of relativistic material, which can cause a re-brightening when a slower more energetic shell of ejecta catches up and re-energizes the decelerating shock front (M. J. Rees & P. Mészáros 1998; R. Sari & P. Mészáros 2000; B. Zhang & P. Mészáros 2002; G. P. Lamb et al. 2019; G. E. Anderson et al. 2025).

R. L. Becerra et al. (2023) highlight that the brightness and timing of GRB 210704A’s excess emission are difficult to explain with standard kilonova and SN scenarios. They suggest an exotic merger channel involving a white dwarf and a compact object (white dwarf, neutron star, or black hole) in a galaxy cluster environment at  $z = 0.2$ . However, they note that this is a poorly constrained scenario and no detailed modelling was performed by them.

In this work, we present multiwavelength observations of GRB 210704A, including those of our own observing campaign. We extend the data set presented by R. L. Becerra et al. (2023) with additional *R/r*- and *K*-band detections and with the *Fermi* Large



**Figure 1.** Top panel: *Fermi*/GBM light curve of GRB 210704A, spanning 8–900 keV and using 64 ms bins (not background-subtracted). Bottom panel: *Fermi*/LAT light curve of GRB 210704A.

Area Telescope (LAT) data (Section 2). We perform independent photometry and data analysis. We line stack our afterglow spectrum and perform spectral energy distribution (SED) fitting, which indicate a redshift of  $z = 2.34$ . Our analysis is presented in Section 3. Additionally, we compare GRB 210704A to other transients, and we use Bayesian inference package REDBACK to model the afterglow and the observed excess emission (Section 4). Finally, we summarize our findings and implications in Section 5.

All magnitudes in this work are in the AB system and upper limits are  $3\sigma$  unless specified differently. We use a flat Lambda cold dark matter cosmology with  $H_0 = 66.7 \text{ km s}^{-1} \text{ Mpc}^{-1}$  and  $\Omega_M = 0.31$  (Planck Collaboration VI 2020). Observation properties are given in the observer frame unless otherwise specified.

## 2 OBSERVATIONS

### 2.1 Gamma-rays

GRB 210704A was discovered by the *Fermi* Gamma-ray Burst Monitor (GBM; C. Meegan et al. 2009) on 2021 July 4 at 19:33:24.59 UT (trigger time  $T_0$ ), with a fluence of  $(1.95 \pm 0.02) \times 10^{-5} \text{ erg cm}^{-2}$  (10–1000 keV and 0.2–1.8 s post-trigger; C. Malacaria, C. Meegan & Fermi GBM Team, 2021). Its prompt emission was also detected by *AGILE* (A. Ursi et al. 2021), *AstroSat* (V. Prasad et al. 2021), *INTEGRAL* (P. Minaev et al. 2021), and *Konus-Wind* (A. Ridnaia et al. 2021). The *Fermi*/GBM light curve in Fig. 1 exhibits a primary emission peak lasting for 2 s, followed by fainter extended emission peaking around 4.5 s. A. Ridnaia et al. (2021) also observe this light curve behaviour with *Konus-Wind*. The extended emission results in a  $T_{90}$  of 4.7 s (50–300 keV),  $4.6^{+2.8}_{-3.6}$  s (20–200 keV), and  $3.5 \pm 0.7$  s (80–8000 keV) for *Fermi*/GBM (C. Malacaria et al. 2021), *AstroSat* (R. L. Becerra et al. 2023), and *INTEGRAL* (P. Minaev et al. 2021), respectively.

This formally places the burst in the long-duration GRB population (C. Kouveliotou et al. 1993), although more accurately it can be classified as an EE-GRB. R. L. Becerra et al. (2023) demonstrate that the extended emission is soft ( $< 300$  keV) compared to the main emission peak. This explains the short duration (1.06 s) reported by A. Ursi et al. (2021) for the *AGILE* observation in its higher energy band of 400 keV–100 MeV.

The spectral lag between the energy bands 25–50 keV and 100–300 keV is  $\tau = 80 \pm 9$  ms (R. L. Becerra et al. 2023).

We analysed the GBM data from the two NaI detectors and the BGO detector with the best viewing angle to the source (n1, n5, and b0). Spectral data files and the corresponding most updated response matrix files (rsp2) are obtained from the online archive.<sup>1</sup> For the time-integrated analysis of the burst (0–4 s from GBM trigger time), we made use of CSPEC data, which have 1024 ms time resolution. We selected the energy channels in the range 10–900 keV for NaI detectors and 0.3–40 MeV for BGO detectors, and we exclude the channels in the range 30–40 keV due to the presence of the Iodine K-edge at 33.17 keV.<sup>2</sup> Spectra were extracted with the public software GTBURST.<sup>3</sup> We discuss the prompt emission spectrum in Section 3.1.

High-energy gamma-rays of GRB 210704A were detected by the *Fermi*/LAT (W. B. Atwood et al. 2009). The LAT is a pair-conversion telescope covering the energy range from 30 MeV to more than 300 GeV. For the extraction and analysis of LAT data, we use GTBURST, following the procedure described in the online official *Fermi* guide<sup>4</sup> and performing an unbinned likelihood analysis.

We select P8R3\_TRANSIENT020 class events, filtering photons in the 100 MeV–20 GeV energy range from a region of interest of  $12^\circ$  radius centred on the burst location. We apply a maximum zenith angle cut of  $100^\circ$  to reduce contamination of gamma-rays from the Earth limb.

We analysed *Fermi*/LAT data over the first 200 s from the GBM trigger time. A time-resolved analysis was performed to characterize the emission at GeV energies and track its temporal evolution. The source is significantly detected [test statistic (TS)  $> 10$ , corresponding to  $\approx 3\sigma$ ] only in the interval 0.75–3.6 s, with TS between 60 and 119. At earlier times (0–0.75 s) and after  $t > T_0 + 3.6$  s, the source is not detected, hence we derived upper limits on the flux. When the source is not detected, the upper limits were computed at 95 per cent confidence level and assuming a photon index fixed to  $-2$ . The *Fermi*/LAT light curve of GRB 210704A is presented in Fig. 1. The reported photon flux above 100 MeV up to  $T_0 + 10$  s is  $F_{\text{ph}} = (1.60 \pm 0.31) \times 10^{-3}$  ph cm $^{-2}$  s $^{-1}$  (A. Berretta et al. 2021).

## 2.2 Follow-up

*Fermi*/LAT and the *Swift* X-Ray Telescope (XRT; D. N. Burrows et al. 2005) facilitated localization efforts (A. Berretta et al. 2021; A. D’Ai et al. 2021), but it ultimately took 0.94 d for the afterglow position to be determined to sub-arcsec precision. This was managed by the 1.5-m AZT-20 telescope of the Assy-Turgen observatory, which determined the location of GRB 210704A to be RA, Dec. =  $10^{\text{h}}36^{\text{m}}04^{\text{s}}.88$ ,  $+57^\circ 12' 58''.5$  in the J2000 frame with an

uncertainty of 0.5 arcsec (V. Kim et al. 2021). Subsequently, we initiated a series of imaging observations with a diverse range of ground-based telescopes, encompassing both visible and IR wavelengths, in addition to triggering afterglow spectroscopy. Furthermore, we initiated target of opportunity (ToO) imaging with the *Hubble Space Telescope* (*HST*). Some of the data have already been reported by R. L. Becerra et al. (2023), but we perform our own independent analysis. All follow-up efforts are detailed below.

### 2.2.1 X-Rays

*Swift*/XRT observed GRB 210704A at four epochs, between 0.6 and 4.5 d after the GBM trigger. We downloaded the high-level data products from the UK Swift Science Data Centre (UKSSDC), which were processed via the techniques described in P. A. Evans et al. (2007, 2009). From a time-averaged XRT spectrum spanning  $T_0 + 53$  ks to  $T_0 + 72$  ks, the UKSSDC reports a photon index of  $\Gamma = 1.5^{+0.6}_{-0.4}$ . Using this  $\Gamma$  and a Galactic column density of  $N_{\text{H}} = 5.59 \times 10^{19}$  cm $^{-2}$ , we correct the fluxes for Galactic extinction using *Chandra*’s Portable, Interactive Multi-Mission Simulator (K. Mukai 1993).

An additional X-ray observation epoch ( $T_0 + 14.4$  d) was obtained with the *Chandra X-ray Observatory* (proposal 22508794, PI: Troja) on 2021 July 19 with the ACIS-S array. The afterglow is detected with 12 counts and a count rate of  $(6.6^{+2.1}_{-1.7}) \times 10^{-4}$  counts s $^{-1}$ , translating to an unabsorbed flux of  $F_{\text{X}} = (1.3^{+0.4}_{-0.3}) \times 10^{-14}$  erg cm $^{-2}$  s $^{-1}$  (0.3–10 keV; R. L. Becerra et al. 2023).

### 2.2.2 Visible bands

For our ground-based follow-up campaign, we initiated visible-band imaging utilizing the Device Optimized for the LOW RESolution (DOLORES) on the 3.6-m Telescopio Nazionale Galileo (TNG; P. D’Avanzo et al. 2021a, b), the 0.8-m T80 at the Observatorio Astrofísico de Javalambre (OAJ; D. A. Kann et al. 2021b), the Calar Alto Faint Object Spectrograph (CAFOS) on the 2.2-m telescope at the Calar Alto Observatory (CAHA; D. A. Kann et al. 2021a), the Optical System for Imaging and low-intermediate-Resolution Integrated Spectroscopy (OSIRIS) mounted on the 10.4-m Gran Telescopio Canarias (GTC; A. De Ugarte Postigo et al. 2021), and the Alhambra Faint Object Spectrograph and Camera (AIFOSC) on the 2.6-m Nordic Optical Telescope (NOT; D. A. Kann et al. 2021c). We include additional images taken with GTC/OSIRIS (A. M. Watson et al. 2021), NOT/ALFOSC, TNG/DOLORES, the Gemini Multi-Object Spectrographs (GMOS) on the 8.1-m Gemini North telescope and the Tiny Wide Field Camera 2 (TWFC2) on the 4.2-m William Herschel Telescope (WHT).

To obtain homogeneous photometry, we process all aforementioned optical observations with our custom photometry pipeline. We use ASTROMETRY.NET (D. Lang et al. 2010) for the astrometric calibration and SEXTRACTOR (E. Bertin & S. Arnouts 1996) for background estimation and source extraction. Using the PHOTUTILS package (L. Bradley et al. 2024), we perform aperture photometry on the background-subtracted images. We use Pan-STARRS DR2 (H. A. Flewelling et al. 2020) for the photometric calibration, selecting six calibration sources when available. We note that we could only use one or two calibration sources for the data from Gemini/GMOS and GTC. All photometry is presented in Table 1.

<sup>1</sup><https://heasarc.gsfc.nasa.gov/W3Browse/fermi/fermigbrst.html>

<sup>2</sup>[https://fermi.gsfc.nasa.gov/ssc/data/analysis/GBM\\_caveats.html](https://fermi.gsfc.nasa.gov/ssc/data/analysis/GBM_caveats.html)

<sup>3</sup><https://fermi.gsfc.nasa.gov/ssc/data/analysis/scitools/gtburst.html>

<sup>4</sup><https://fermi.gsfc.nasa.gov/ssc/data/analysis/scitools/gtburst.html>

**Table 1.** Post-GRB photometry, not corrected for extinction. Listed are the time since the burst (using the mid-exposure time) in days, the exposure time in seconds, the telescope/instrument, the observation filter, the AB magnitude of the detection or  $3\sigma$  upper limit (indicated with the  $>$ -symbol) and the reference for the photometry.

$t_{\text{mid}} - T_0$ (d)	$t_{\text{exp}}$ (s)	Instrument	Band	Magnitude (AB)	Reference
0.391	360	DDOTI	<i>w</i>	$> 20.3$	S. Dichiaro et al. (2021)
0.726	3038	Swift/UVOT	<i>V</i>	$> 21.1$	A. A. Breeveld, A. Y. Lien & Swift/UVOT Team, (2021)
0.944	3960	AZT-20	<i>r'</i>	$22.25 \pm 0.13$	V. Kim et al. (2021)
1.080	1800	TNG/DOLORES	<i>r</i>	$22.50 \pm 0.07$	This work
1.081	900	OAJ/T80Cam	<i>z'</i>	$> 21.4$	This work
1.093	1500	CAHA-2.2m/CAFOS	<i>i</i>	$21.66 \pm 0.29$	This work
1.093	600	OAJ/T80Cam	<i>i'</i>	$22.26 \pm 0.46$	This work
1.094	60	GTC/OSIRIS	<i>r'</i>	$22.24 \pm 0.09$	This work
1.099	1200	WHT/TWFC2	<i>r</i>	$22.74 \pm 0.05$	This work
1.104	900	OAJ/T80Cam	<i>g'</i>	$22.84 \pm 0.29$	This work
1.113	1200	WHT/TWFC2	<i>z</i>	$> 22.6$	This work
1.116	900	OAJ/T80Cam	<i>r'</i>	$22.63 \pm 0.26$	This work
1.29	1152	HJT/RATIR	<i>r</i>	$> 22.4$	R. L. Becerra et al. (2023)
1.29	1152	HJT/RATIR	<i>i</i>	$> 22.1$	R. L. Becerra et al. (2023)
2.062	2700	CAHA-2.2m/CAFOS	<i>r</i>	$> 22.7$	T. R. Sun et al. (2021)
2.096	1200	WHT/TWFC2	<i>z</i>	$> 22.6$	This work
2.104	420	GTC/OSIRIS	<i>r'</i>	$23.63 \pm 0.11$	This work
2.107	540	GTC/OSIRIS	<i>z'</i>	$23.69 \pm 0.46$	This work
2.114	1600	WHT/TWFC2	<i>r</i>	$23.33 \pm 0.11$	This work
3.920	4620	AZT-20	<i>r'</i>	$> 23.1$	N. Pankov et al. (2021)
4.095	2700	TNG/DOLORES	<i>i</i>	$24.08 \pm 0.28$	This work
4.122	900	TNG/DOLORES	<i>r</i>	$23.83 \pm 0.30$	This work
4.457	840	Gemini North/NIRI	<i>K</i>	$23.18 \pm 0.08$	This work
5.117	1080	GTC/OSIRIS	<i>r'</i>	$23.48 \pm 0.08$	This work
5.119	840	GTC/OSIRIS	<i>z'</i>	$22.59 \pm 0.17$	This work
5.447	1440	Gemini North/NIRI	<i>J</i>	$22.88 \pm 0.21$	This work
5.474	1980	Gemini North/NIRI	<i>K</i>	$23.35 \pm 0.23$	This work
6.086	900	NOT/ALFOSC	<i>g'</i>	$23.61 \pm 0.17$	This work
6.097	900	NOT/ALFOSC	<i>r'</i>	$23.52 \pm 0.15$	This work
6.35	1500	LDT/LMI	<i>r</i>	$23.14 \pm 0.27$	R. L. Becerra et al. (2023)
6.451	2220	Gemini North/NIRI	<i>K</i>	$23.07 \pm 0.10$	This work
6.983	3600	Zeiss-1000	<i>R</i>	$23.1 \pm 0.3$	A. Volnova et al. (2021)
7.468	660	Gemini North/NIRI	<i>K</i>	$22.53 \pm 0.29$	This work
8.946	7200	Zeiss-1000	<i>R</i>	$> 23.5$	A. Volnova et al. (2021)
10.448	1080	Gemini North/GMOS	<i>r</i>	$23.16 \pm 0.43$	This work
11.44	900	Gemini North/GMOS	<i>z</i>	$> 22.44$	R. L. Becerra et al. (2023)
12.451	1740	Gemini North/NIRI	<i>K</i>	$22.73 \pm 0.07$	This work
13.091	2100	TNG/DOLORES	<i>r</i>	$> 23.3$	This work
14.449	1584	Gemini North/GMOS	<i>z</i>	$24.10 \pm 0.19$	This work
30.081	600	NOT/ALFOSC	<i>R</i>	$> 24.0$	This work
32.088	900	NOT/ALFOSC	<i>R</i>	$24.18 \pm 0.38$	This work
115.00	3030	Subaru/HSC	<i>r</i>	$> 25.21$	R. L. Becerra et al. (2023)
160.796	7140	Gemini North/NIRI	<i>K</i>	$24.65 \pm 0.18$	This work

We supplement our data with photometry from General Coordinates Network reports, taken with the *Swift* Ultra-Violet/Optical Telescope (UVOT; P. W. A. Roming et al. 2005), the AZT-20 telescope of the Assy-Turgen observatory, the Reionization And Transients IR camera (RATIR) on the Harold Johnson Telescope (HJT) at the Observatorio Astronómico Nacional San Pedro Mártir (OAN-SPM), the 2.2-m telescope at CAHA, the Large Monolithic Imager (LMI) on the Lowell Discovery Telescope (LDT), the Zeiss-1000 telescope of the Special Astrophysical Observatory of the Russian Academy of Science (SAO RAS), GMOS on Gemini North and the Hyper Suprime-Cam (HSC) on the Subaru telescope. S. Dichiaro et al. (2021) also obtained a  $5\sigma$ -upper limit with the Deca-Degree Optical Transient Imager (DDOTI) at the OAN-SPM, which we convert to a  $3\sigma$ -limiting magnitude with an additional term of  $-2.5 \log_{10}(3/5)$ . This sup-

plemental photometry is listed in Table 1 along with the appropriate references.

### 2.2.3 Infrared

GRB 210704A was observed by the Gemini Near-IR Imager (NIRI) mounted on Gemini North, for six epochs in *K* and one epoch in *J*. We reduce the images using the DRAGONS pipeline (Data Reduction for Astronomy from Gemini Observatory North and South; K. Labrie et al. 2023), employing IRAF (Image Reduction and Analysis Facility; D. Tody 1986, 1993; M. Fitzpatrick et al. 2025) for the astrometry. We then use the HOTPANTS routine (High Order Transform of Point-spread function ANd Template Subtraction; A. Becker 2015) to subtract the last *K*-band epoch

**Table 2.** Late-time *HST* photometry at the location of GRB 210704A, not corrected for extinction. Listed are the telescope channel, observation band, observation date, time since the GRB (using the start of the exposure) in days, the AB magnitudes using a 1-arcsec aperture and the AB magnitudes using a 0.2-arcsec aperture. Upper limits are  $2\sigma$  and indicated with the  $>$ -symbol.

Channel	Band	Observation date	$t_{\text{start}} - T_0$ (d)	Magnitude (1 arcsec)	Magnitude (0.2 arcsec)
UVIS	F336W	2022 Jan 14	193.95	$> 25.7$	$26.81 \pm 0.35$
UVIS	F438W	2022 Jan 14	194.02	$> 25.4$	$26.74 \pm 0.25$
UVIS	F606W	2022 Jan 14	194.08	$25.16 \pm 0.17$	$25.99 \pm 0.04$
IR	F105W	2021 Oct 19	107.18	$25.06 \pm 0.28$	$25.69 \pm 0.08$
IR	F160W	2021 Oct 19	107.17	$24.06 \pm 0.14$	$24.57 \pm 0.06$

( $T_0 + 161$  d) from the other *K*-band stacks. For the *K*-band epochs 4, 6, and 12 d after the burst, this results in a clean image that we use for the photometry instead of the image stack itself. We perform aperture photometry, calibrated to 2MASS (Two Micron All Sky Survey; M. F. Skrutskie et al. 2006). The IR photometry is listed in Table 1.

### 2.2.4 Afterglow spectrum

We took  $4 \times 600$  s spectra with OSIRIS mounted on the 10.4-m GTC telescope at Roque de los Muchachos Observatory, on the island of La Palma (Spain). The spectra were obtained using the R1000B grism, which covers the wavelength range 3700–7800 Å, as reported by A. De Ugarte Postigo et al. (2021). The slit was placed in the parallactic angle to avoid differential slit losses, with a width of 1 arcsec, resulting in a spectral resolving power of around 600. The combined spectrum was obtained at an average epoch of 26.75 h after the burst. The spectrum was reduced using self-developed pipelines that include bias and response correction, wavelength calibration, and flux calibration using the spectrophotometric standard Ross 640 as reference. The spectrum is discussed in Section 3.3.

### 2.2.5 Late-time host spectrum

On 2022 February 5 (216 d after the GRB), a set of six spectroscopic exposures of 1200 s each were performed with the twin Multi-Object Double Spectrograph MODS-1 and MODS-2 (R. W. Pogge et al. 2010) mounted on the Large Binocular Telescope (LBT) on Mt. Graham (Arizona, USA). We used the dual-grating mode, which provided a wavelength coverage of 3200–9500 Å, and a slit mask with a width of 1.2 arcsec. The slit was positioned on the GRB location and oriented with a position angle of  $40^\circ 9'$  to keep the bright star used for the acquisition in the slit, useful for a precise control of the target placement.

Observations were obtained at an average airmass of 1.5, seeing  $\approx 0.8$  arcsec, and clear sky conditions.

We processed the LBT spectrum using the Spectroscopic Interactive Pipeline and Graphical Interface tool (A. Gargiulo et al. 2022) and performed wavelength calibration using arc lamp frames. To obtain flux-calibrated LBT spectra, we applied the sensitivity function derived from the spectrophotometric standard star GD 71. Only the first  $4 \times 1200$  s exposures were stacked in the blue side (3200–5600 Å) because of increasing sky background during morning twilight. Unfortunately, since MODS is not equipped with an atmospheric dispersion corrector (ADC), the signal blueward of 4400 Å was lost due to atmospheric dispersion.

**Table 3.** Pre-GRB photometry of the source underlying GRB 210704A, not corrected for extinction. Listed are the telescope/instrument, observation band and AB magnitude. The upper limit is  $3\sigma$  and indicated with an  $>$ -symbol.

Telescope	Band	Magnitude (AB)
CFHT/MegaCam	<i>u</i> (MP9301)	$26.51 \pm 0.57$
CFHT/MegaCam	<i>g</i> (MP9401)	$24.99 \pm 0.24$
CFHT/MegaCam	<i>r</i> (MP9601)	$25.38 \pm 0.19$
CFHT/MegaCam	<i>i</i> (MP9701)	$25.48 \pm 0.35$
CFHT/MegaCam	<i>z</i> (MP9801)	$> 23.6$
Subaru/HSC	<i>g</i>	$25.57 \pm 0.08$
Subaru/HSC	<i>i</i>	$25.54 \pm 0.18$
Subaru/HSC	<i>z</i>	$25.63 \pm 0.42$

### 2.2.6 Late-time *HST* observations

Following our ToO (*HST* proposal 16275, PI: Tanvir), the field of GRB 210704A was observed by *HST* on 2021 October 19 using the IR channel of Wide Field Camera 3 (WFC3) and on 2022 January 14 with the UVIS channel of WFC3. A log of the observations is shown in Table 2. The images are reduced via ASTRODRIZZLE (R. J. Avila et al. 2015) with the final pixel scale set to  $0.07$  arcsec pixel $^{-1}$  for the IR channel and  $0.025$  arcsec pixel $^{-1}$  for the UVIS channel. For the astrometry, we use our Gemini/NIRI images.

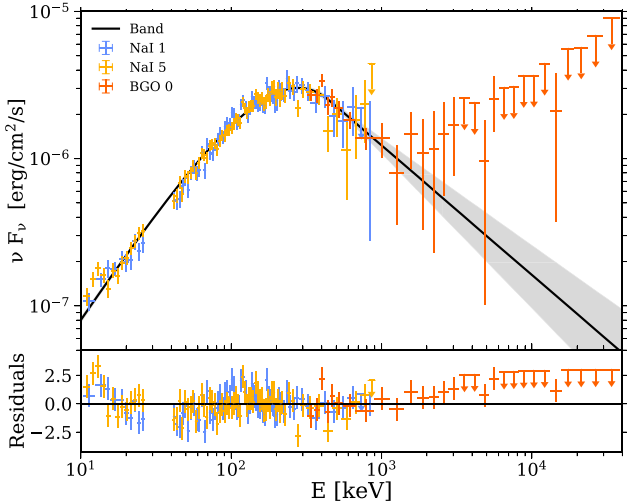
## 2.3 Archival data

The location of GRB 210704A was observed between 2003 and 2012 – well before the GRB – by the Canada–France–Hawaii Telescope (CFHT) in *u*, *g*, *r*, *i*, and *z* using its MegaPrime imager. Additionally, there are pre-burst archival data taken with the Subaru telescope (in *g*, *i*, and *z*) in the Hyper Suprime-Cam Legacy Archive 2016 (HSCLA; M. Tanaka et al. 2021). We run the image stacks through our photometry pipeline, where we use SDSS DR19 (SDSS Collaboration 2025) for the photometric calibration of the *u*-band image and Pan-STARRS DR2 (H. A. Flewelling et al. 2020) for the other data. A source is detected at the location of the GRB (Table 3).

## 3 RESULTS

### 3.1 *Fermi* observations

We perform a spectral analysis of the prompt *Fermi*/GBM data with the public software XSPEC (v. 12.12.1). We fit a Band function to the *Fermi*/GBM energy spectrum of the initial 4 s of prompt emission (Fig. 2). We use the PG-Statistic in the fitting procedure, which is valid for Poisson data with a Gaussian background.



**Figure 2.** The upper panel shows the *Fermi*/GBM spectrum (data points) integrated over the first 4 s of GRB 210704A, overlaid with the best-fitting model (Band; solid graph) and the 16th to 84th percentile model uncertainty interval (shaded region). The lower panel shows the residuals of the fit.

The fit yields  $E_{\text{peak}} = 280 \pm 10$  keV and power-law indices  $\alpha = -0.46 \pm 0.03$  and  $\beta = -2.86 \pm 0.16$ . Analysing the *Fermi*/LAT data from the same initial 4 s gives a hard power-law spectral index of  $-1.64 \pm 0.14$ . This hardness contrasts with the significantly softer  $\beta$  from the GBM data. Therefore, the LAT emission does not lie on the extrapolation of the lower energy GBM spectrum, indicating the presence of an additional harder spectral component at GeV energies. To investigate whether this could be high-energy emission from the GRB afterglow, we include the LAT data in our afterglow modelling in Section 4.4. Although high-energy afterglow emission is not common, it has been observed before in LAT data (e.g. G. Ghirlanda, G. Ghisellini & L. Nava 2010).

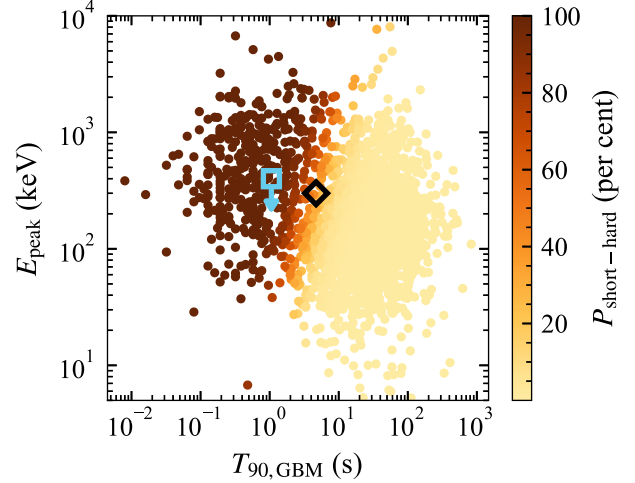
We compare the peak energy and duration of GRB 210704A to the GRB population in Fig. 3. The GRBs in the figure cluster into two groups: short-hard (top left) and long-soft bursts (bottom right). GRB 210704A (diamond) lies on the transition area between the groups, where it is formally classified as a long-soft burst, as  $P_{\text{long-soft}} = 66$  per cent. Alternatively, using the duration determined with *AGILE* ( $T_{90} = 1.06$  s in 400 keV–100 MeV), which excludes the softer extended emission, GRB 210704A would be classified as a short-hard burst (square).

The *Fermi*/LAT emission of GRB 210704A is delayed by 0.75 s with respect to the *Fermi*/GBM emission. Comparing GRB 210704A’s onset time and duration to other LAT bursts shows that it lies on the periphery of the LGRB population (Fig. 4, diamond). GRB 210704A’s onset time is representative of the bottom 20 per cent of the LAT population, yet is within the range of both SGRBs and LGRBs. When excluding the extended emission, GRB 210704A is consistent with the SGRB population (square).

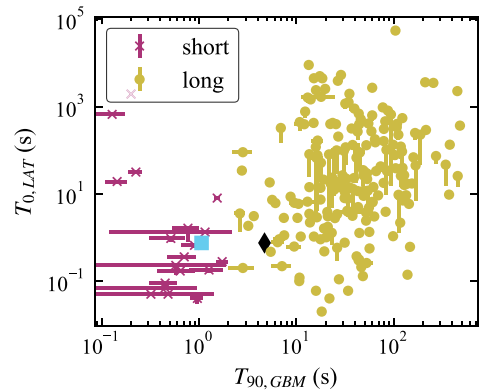
In both figures, the extended emission strongly affects the classification of GRB 210704A.

### 3.2 Environment

GRB 210704A is located in a significant galaxy overdensity (Fig. 5), which we previously reported in A. J. Levan et al. (2021). In particular, the *HST* image overlaps with galaxy cluster 400d



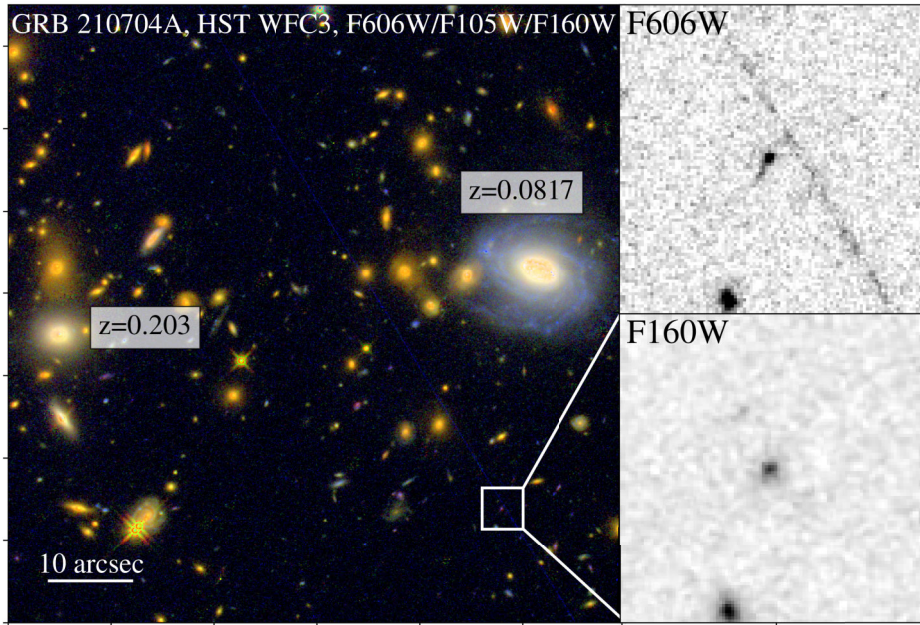
**Figure 3.** Peak energy versus duration (50–300 keV) for the 2308 GRBs from the Fourth *Fermi*/GBM GRB Catalog (D. Gruber et al. 2014; A. Von Kienlin et al. 2014, 2020; P. Narayana Bhat et al. 2016).  $E_{\text{peak}}$  is determined with a Band-function fit to a single spectrum over the duration of each burst. The bursts cluster into two groups: short-hard GRBs (top left) and long-soft GRBs (bottom right). Following T. Ahumada et al. (2021), we fit two lognormal distributions to the data to determine the probability of each burst belonging to the cluster of short-hard bursts. This sets the colour scale. GRB 210704A is marked by a diamond. The square is GRB 210704A as observed by *AGILE*, or in other words, disregarding the extended emission. As the energy peak is not observed in the *AGILE* energy range, the square represents an upper limit. All values are in the observer frame.



**Figure 4.** Onset time of the LAT emission (100 MeV–100 GeV) versus duration (50–300 keV) for SGRBs and LGRBs from the Second *Fermi*/LAT GRB Catalog (M. Ajello et al. 2019). The onset time is defined as the time when the first photon with probability  $> 0.9$  of being associated with the GRB is detected in the 100 MeV–100 GeV range. GRB 210704A is marked by a diamond. The square is GRB 210704A when disregarding the extended emission. All values are in the observer frame.

J1036+5713 at  $z = 0.203$  (C. R. Mullis et al. 2003). At this redshift, the isotropic equivalent energy of GRB 210704A would be  $E_{\text{iso}} = 2 \times 10^{51}$  erg. The nearest galaxies of the cluster are within a few arcsec of the GRB.

Furthermore, GRB 210704A is 45 kpc (30 arcsec) away from spiral galaxy WISEA J103604.24+571327.7, which has an absolute magnitude of  $-21.97 \pm 0.50$  mag, a reported apparent magnitude of  $i = 15.962 \pm 0.007$  mag (K. Abazajian et al. 2004), and



**Figure 5.** **Left:** colour-composite image of the environment of GRB 210704A, made from *HST* data. The GRB location is marked by the box. The spiral galaxy on the right side of the image is foreground galaxy WISEA J103604.24+571327.7 at a redshift of  $z = 0.0817$ , at a distance of 30 arcsec (45 kpc) from GRB 210704A. The *HST* image also overlaps with galaxy cluster 400d J1036+5713 at  $z = 0.203$ . **Right:** zoomed-in region around the GRB position showing the galaxy underlying the GRB in the F606W and F160W filters. While in F160W the source is dominated by a compact core, in F606W there is an apparent extension and an irregular morphology. Archival optical imaging suggests that the light observed in F606W is dominated by the galaxy, but a transient contribution is possible in the F160W images.

a redshift of  $z = 0.0817$  (K. Abazajian et al. 2004; F. D. Albareti et al. 2017), where  $E_{\text{iso}} = 3 \times 10^{50}$  erg.

Finally, the pre-burst CFHT and Subaru data indicate the presence of a source at the location of GRB 210704A that is observationally red ( $u - r = 1.1 \pm 0.6$ ). The late-time *HST* F606W image (Fig. 5) reveals a relatively complex emission region, where the burst is consistent with a compact knot of emission that is marginally extended (major axis is 0.13 arcsec), along with a more extended component to the south-east. The extended morphology may be indicative of an underlying galaxy. Table 2 presents *HST* photometry using a narrow 0.2-arcsec aperture centred on the bright knot, as well as a larger 1-arcsec aperture. The complex nature of the emission is discussed in more detail in Section 4.3.

R. L. Becerra et al. (2023) calculate a chance alignment probability of  $P_{\text{chance}} = 0.02$  for the underlying source,  $P_{\text{chance}} = 0.05$  for the galaxy at  $z = 0.0817$ , and  $P_{\text{chance}} = 0.012$  for the cluster at  $z = 0.203$  (or  $10^{-3}$  when factoring in cluster brightness and applying a cut on X-ray flux).

### 3.3 Redshift

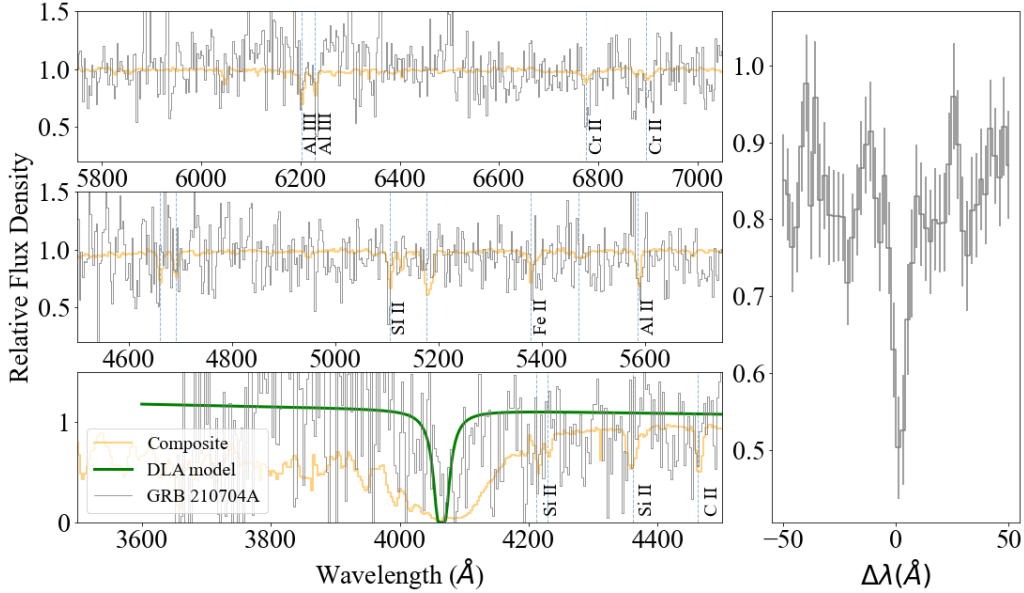
In our GTC afterglow spectrum taken at  $T_0 + 1.1$  d (Fig. 6), we detect a continuum down to 3800 Å, which gives an upper limit on the redshift of  $z < 3.17$ . The signal-to-noise ratio (S/N) of the afterglow spectrum is low (in the range  $3\sigma$ – $5\sigma$  per pixel over wavelengths 4000–7500 Å) and even lower at the blue end ( $\lambda < 4000$  Å), where the flux calibration is also less reliable. We find a broad dip at  $\approx 4050$  Å, which we tentatively interpret as Ly  $\alpha$  absorption. This implies a redshift of  $z = 2.34$ . Low-significance detections of Si II and C II are consistent with this redshift. C IV and Si IV are not detected, although the latter is not unprecedented. We measure for C II and C IV rest-frame equivalent widths

of  $1.3 \pm 0.4$  Å and  $< 1.2$  Å ( $3\sigma$  upper limit), respectively. Comparing these measurement with Fig. 8 of A. Ugarte Postigo et al. (2012), we can see that, due to the low S/N, the non-detection of C IV is not constraining.

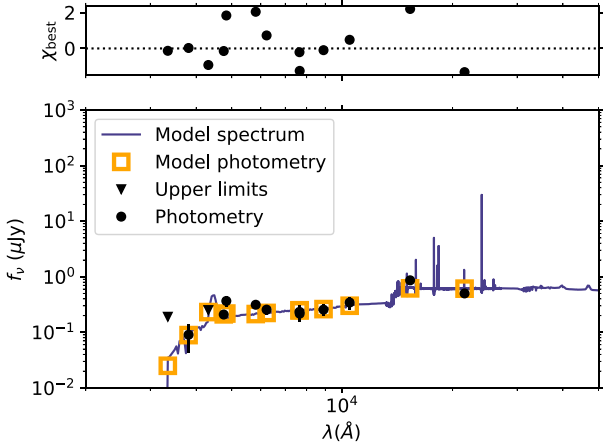
To consolidate the identification of the spectral lines, we also performed line-stacking analysis. In particular, we stack the low-ionization metal lines with an equivalent width  $> 0.5$  Å based on the line-strength measurements in the composite GRB spectrum of L. Christensen et al. (2011). Due to its proximity to an atmospheric skyline, we omit from the stack Al II. The result is shown in the right panel of Fig. 6. The stacked data indicate a clear absorption feature, corroborating our spectral analysis. Combined with the presence of Ly  $\alpha$  absorption this provides high confidence in the redshift.

The late-time LBT host spectrum reveals weak continuum over the range 4500–9200 Å. No emission lines are however visible over this range. This is in fact consistent with the absorption redshift, since at  $z = 2.34$  none of the brighter lines falls in the covered range, thus providing further support for the GTC value.

To check, we also determine a photometric redshift for the underlying source with PROSPECTOR (J. Leja et al. 2017; B. D. Johnson et al. 2021), combining the pre-burst CFHT and Subaru observations, the *HST* photometry taken 107 and 194 d post-trigger using 1-arcsec apertures, and the Gemini *K*-band detection from  $T_0 + 161$  d. We use the delayed-exponential parametric star formation history model, which describes the star formation rate as linearly rising followed by an exponential decline with time. From the SED fit (Fig. 7), we derive a redshift of  $z = 2.63^{+0.21}_{-1.34}$  (68 per cent credible interval). The resulting fit parameters suggest a galaxy of low mass [ $\log_{10}(M/M_{\odot}) \approx 9.6$ ] and low metallicity ( $Z \approx 0.02 Z_{\odot}$ ), with a relatively young stellar population ( $t \approx 0.3$  Gyr) and moderate extinction  $A_V \approx 1.0$ . This is consistent



**Figure 6.** GTC afterglow spectrum of GRB 210704A. The spectrum is split in wavelength over the three panels on the left. The lower panel includes a damped Ly  $\alpha$  model. The composite spectrum (L. Christensen et al. 2011) is also shown. We note that flux calibration is poor below  $\approx 4000$  Å. The right panel displays the stack of lines, using a width of  $100$  Å around all the lines labelled in one of the left three panels. Note that the Al II line has been omitted from this stack due to a proximate skyline.



**Figure 7.** SED fit to the galaxy underlying GRB 210704A, using 1-arcsec aperture *HST* photometry, the Gemini *K*-band detection at 161 d and the archival CFHT and Subaru data. The dotted line in the upper panel corresponds to  $\chi_{\text{best}}^2 = 0$ , the squared mean is  $\chi_{\text{best,avg}}^2 = 0.06$ .

with the hosts of core-collapse GRB progenitors (J. T. Palmerio et al. 2019), as is the case for GRB 210704A’s position with respect to the underlying source, its spectral lag ( $\tau = 80 \pm 9$  ms; R. L. Becerra et al. 2023), its  $E_{\text{iso}} = 2 \times 10^{53}$  erg, and its location on the Amati relation at  $z = 2.34$ . This is indicative of a core-collapse progenitor rather than a compact object merger, which is atypical for an EE-GRB.

When we use the more narrow 0.2-arcsec apertures for the *HST* data instead, we obtain consistent SED fit parameters. Setting the redshift to  $z = 2.34$  in the SED fitting also gives consistent galaxy properties.

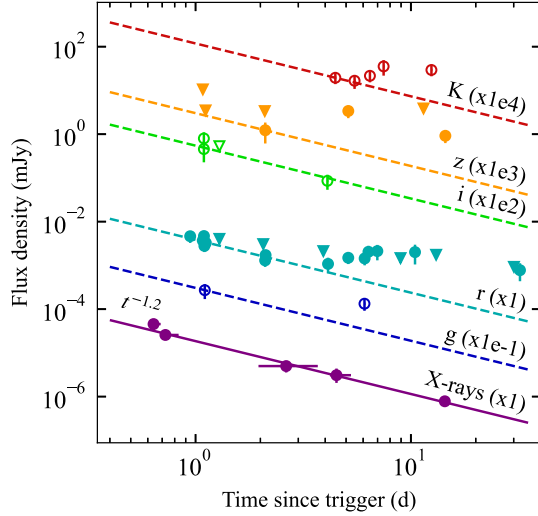
The photometric redshift of the underlying source is consistent with the tentative redshift derived from the afterglow spectrum, thereby reinforcing the credibility of the spectroscopic redshift.

We thus consider  $z = 2.34$  as the redshift of GRB 210704A for our further analysis.

### 3.4 Light curve: optical/IR excess

For the light curve analysis in this paper, we correct the photometry in Table 1 for Galactic extinction  $E(B - V) = 0.007$  (G. M. Green et al. 2015), following E. F. Schlafly & D. P. Finkbeiner (2011) to obtain the true extinction per band. To account for filter differences and uncertainties in the data reduction, we add an extra systematic error of 0.3 mag in quadrature to the optical/IR photometry. The light curve of GRB 210704A is presented in Fig. 8. The solid line represents the best-fitting power law for the five X-ray detections, with an index of  $\alpha = -1.2 \pm 0.1$  ( $\chi_{\text{red}}^2 = 0.6$ ;  $F_X \propto t^\alpha$ ). This index is consistent with typical GRB afterglows (B. Zhang et al. 2006) and yields an electron index of  $p = 2.6$  (assuming a uniform medium and the slow-cooling regime). The dashed lines in the figure indicate power laws with the same index fitted to the data of the other bands. Excess emission with respect to the power-law afterglow is evident in all visible and IR bands except *i*, for which we do not have data at the time of the excess. The excess in the *r* band starts after 4–5 d, while in the *K*-band it appears to be moderately delayed by  $\approx 1.5$  d. The observed peak of the excess is at  $T_0 + 7$  d (2 d in the rest frame), reaching an absolute magnitude of  $M_r = -22.0$  mag. This is significantly brighter than the pre-burst CFHT data ( $\Delta m_r = 2.3 \pm 0.5$  mag). The upper limit reported by A. Volnova et al. (2021) suggests that the observed peak closely approximates the true peak in *r*. However, due to the limited IR coverage, we can only set limits on the true peak absolute magnitude,  $M_K \leq -22.6$  mag, and peak time, 7–12 d, in *K* (rest-frame *r*).

Fig. 9 shows the colour evolution of GRB 210704A, where the lower panel shows the optical/IR SEDs and the upper panel includes the X-ray detections. Due to the limited number of simultaneous observations, we group the detections in temporal

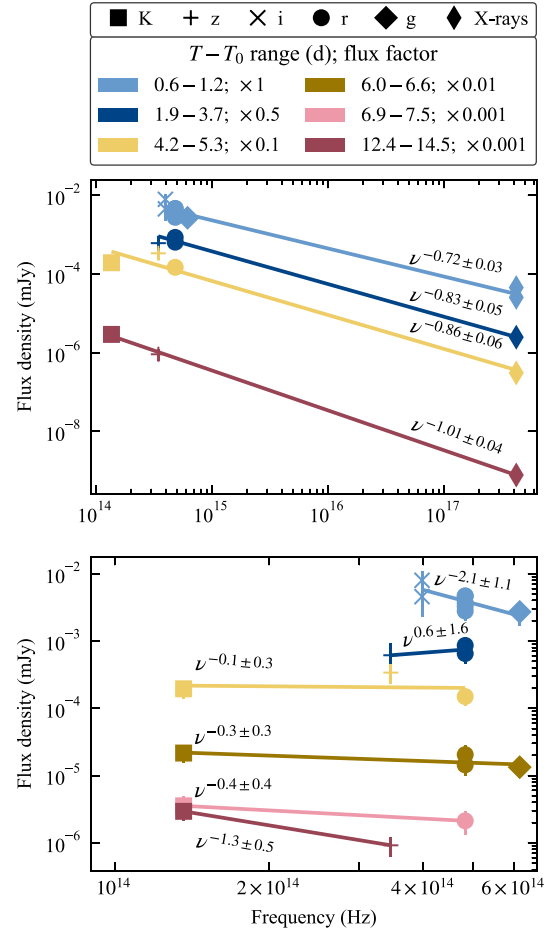


**Figure 8.** Light curve of GRB 210704A in different bands in the observer frame. The flux for the visible and IR bands are multiplied with arbitrary powers of 10, as indicated in the brackets on the right, to visually separate them in the figure. Open and closed symbols are alternated per filter for visual clarity. Upper limits are given as triangles. The X-ray data can be fitted with a power law with index  $\alpha = -1.2$ , shown with the solid line. A power law with the same index is fitted to the pre-excess data of the other bands (dashed lines).

bins (we note that because the behaviour is not monotonic, interpolating to a fixed time is not straightforward). We adopt a default bin width of 0.6 d, but extend the second and third epochs to span the full *Swift*/XRT observing intervals, yielding widths of 1.8 and 1.1 d, respectively. Additionally, we include a wide late-time bin spanning 12.4–14.5 d that covers the K-band detection at 12.4 d and the z-band and X-ray data at 14.2–14.5 d. We note that although the inclusion of the K-band observation broadens the later time bin, excluding it yields a similar optical/IR to X-ray SED (upper panel of Fig. 9). A power law ( $f \propto \nu^\beta$ ) is fitted to the data of each time bin, yielding spectral indices  $\beta_{\text{ox}}$  and  $\beta_{\text{op}}$  for the upper and lower panel, respectively.

In the early afterglow phase ( $< 3.7$  d), a power-law fit to the X-ray and optical/IR data yields a spectral index of  $\beta_{\text{ox}} = -0.75 \pm 0.03$  (weighted average with  $\chi^2_{\text{red}} = 3.6$ ;  $f_{\nu} \propto \nu^{\beta_{\text{ox}}}$ ). This is consistent with the power-law slopes of the X-ray spectra ( $\beta_X = -0.5^{+0.4}_{-0.6}$  and  $\beta_X = -0.7^{+1.2}_{-2.3}$  for 0.6–1.2 and 1.9–3.7 d, respectively), although we note the substantial errors in the latter. Moreover, it is consistent with non-thermal synchrotron emission from a standard GRB afterglow (M. De Pasquale et al. 2003) and the spectral index that can be derived from closure relations:  $\beta = 2\alpha/3 = -0.8$  (assuming a uniform medium and the slow-cooling regime). The optical/IR spectral index  $\beta_{\text{op}} = -1.2 \pm 0.9$  (weighted average,  $\chi^2_{\text{red}} = 1.8$ ) is poorly determined, but consistent with  $\beta_{\text{ox}}$ . This supports a single synchrotron component across the IR to X-ray bands at early times.

The X-ray and optical/IR light curves decouple after  $\approx 4$  d (Fig. 8). Although no X-ray observations were taken around the light-curve peak, interpolating the X-ray flux density to 7.2 d using  $\alpha = -1.2$  yields a steeper spectral index of  $\beta_{\text{ox}} \approx -1$  at 6.9–7.5 d. At later times (12.4–14.5 d),  $\beta_{\text{ox}}$  remains consistent with this steeper index (Fig. 9). The optical/IR spectral index  $\beta_{\text{op}}$  remains unchanged during the excess emission phase up to 7.5 d, beyond which the large uncertainties limit further interpretation (Fig. 9).



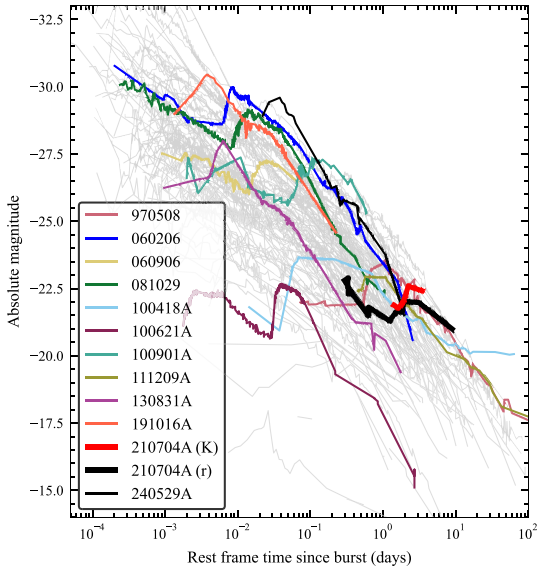
**Figure 9.** Colour evolution of GRB 210704A. The upper panel includes X-ray data. The lower panel only contains visible- and IR-band data. In both panels, the time bins are chronologically ordered from top to bottom and visually separated by multiplying the fluxes with the flux factor listed in the legend. A power law ( $f \propto \nu^\beta$ ) is fitted to the data of each time bin. The time bins 0.6–1.2 d and 1.9–3.7 d post-GRB correspond to the early afterglow phase. The bin of 6.9–7.5 d is the bin around the peak of the excess emission.

The observed spectral steepening could represent the emergence of a new optical/IR emission component. Alternatively, it could be caused by a cooling break starting to pass through the X-ray band. Although there is no evidence for such a break in the X-ray light curve (Fig. 8), the sparse light curve does allow for a cooling break in combination with a refreshed shock, as will be discussed in Section 4.4.2.

To further investigate the excess emission, we determine the rise time  $t_{1/2, \text{rise}}$  from half-maximum flux density to peak by linearly interpolating the K-band light curve, following D. A. Perley et al. (2020) and A. Y. Q. Ho et al. (2023). Using linear extrapolation, we also determine the fade time  $t_{1/2, \text{fade}}$  of the excess emission. The sum of the rise and fade time gives us the duration of the excess above the half-maximum flux. The results are listed in Table 4. We discuss the duration of the excess further in the next section.

**Table 4.** Rise and fade times with respect to half-maximum flux for GRB 210704A and two *Einstein Probe* transients, in the observer frame and in the band closest to rest-frame  $g$ . The sum of the rise and fade time, which is the duration of the transient above half-maximum flux, is listed in the last column (in days).

Transient	Band	$t_{1/2,\text{rise}}$ (d)	$t_{1/2,\text{fade}}$ (d)	$\Delta t$ (d)
GRB 210704A	$K$	$1.8 \pm 0.6$	$14.8 \pm 6.4$	$16.6 \pm 6.4$
EP240414a	$r$	$1.2 \pm 0.1$	$1.3 \pm 0.4$	$2.5 \pm 0.4$
EP241021a	$z$	$2.0 \pm 0.2$	$5.7 \pm 1.1$	$7.7 \pm 1.1$



**Figure 10.** Kann plot comparing the light curve of GRB 210704A in the  $r$ band (rest-frame UV) and in the  $K$ band (rest-frame  $r$ ) to the light curves of GRBs. The non-highlighted light curves are from D. A. Kann et al. (2011) in  $Rc$ , just like the light curves of GRBs 970508, 060206, 060906, 081029, 100621A, and 100901A which are highlighted in colour as they undergo rebrightening episodes. Other rebrightening bursts that are included are GRBs 100418A ( $r'/R$ ; A. Ugarte Postigo et al. 2018), 111209A ( $r'$ ; D. A. Kann et al. 2018), 130831A ( $V$ ; M. De Pasquale et al. 2016), 191016A ( $r$ ; M. Pereyra et al. 2022), and 240529A ( $r/R$ ; T.-R. Sun et al. 2024). Light curves are not corrected for host galaxy extinction.

## 4 DISCUSSION

### 4.1 Comparing GRB 210704A to other GRBs

In principle, the rise of the light curve to a later peak might be the result of viewing a GRB off-axis. However, the rapid rise of the afterglow in the optical/IR excludes this scenario.

The Kann plot in Fig. 10 shows that GRB 210704A starts off as an average afterglow, but due to the excess emission it becomes as bright as the brightest afterglows observed. The excess corresponds to an observed luminosity increase of  $0.62 \pm 0.24$  mag in  $K$  and  $0.69 \pm 0.40$  mag in  $r$ . This is both consistent with a rebrightening as well as with a flattening (within  $3\sigma$ ) of the light curve. Late-time flattening in GRB light curves is typically due to host emission, but that is not the case here as the CFHT data reveal a much fainter underlying galaxy ( $\Delta m_r = 2.3 \pm 0.5$  mag). Late-time light curve plateaus can also be driven by the same physical mechanisms responsible for rebrightenings, but with a reduced energy input. For instance, refreshed shocks have been proposed to explain the plateau phase of GRB 191016A around 0.02 rest-frame days (Fig. 10; M. Pereyra et al. 2022).

The coloured graphs in Fig. 10 show GRBs that undergo rebrightening episodes. The rebrightening typically occurs during the first rest-frame day and corresponds to a luminosity increase of 1–3 mag. GRBs with multiband data show that the colour of the emission is bluer before the rebrightening (e.g. GRBs 081029, 100621A, and 111209A; A. Ugarte Postigo et al. 2018). While the observed light curve of GRB 210704A could be consistent with a rebrightening and reddening, the photometric uncertainties preclude a definitive match with these properties of rebrightening GRBs. GRB 210704A’s excess emission also rises later than the rebrightening GRBs in Fig. 10. The physical origin of rebrightenings in GRBs remains debated, but proposed models for the highlighted rebrightening GRBs in Fig. 10 include refreshed shocks (e.g. GRB 100621A; J. Greiner et al. 2013) or a CSM density bump (e.g. GRB 970508; P. H. Tam et al. 2005). Section 4.4 further examines these models in the context of GRB 210704A.

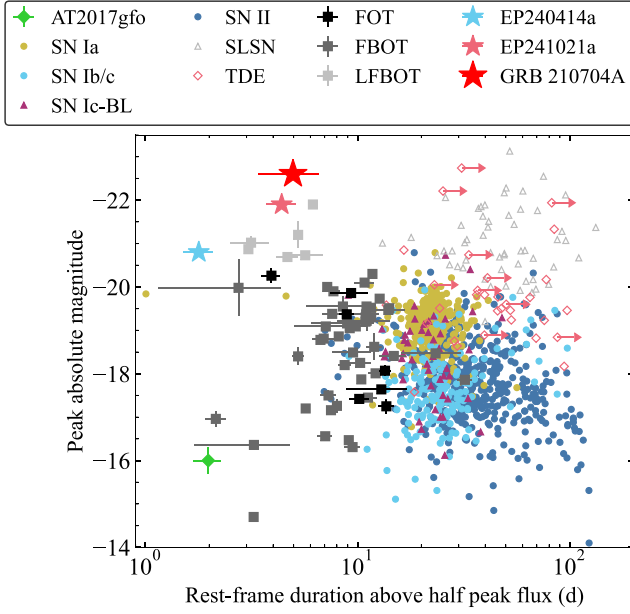
### 4.2 Comparing GRB 210704A’s excess emission to other transient populations

A light curve rise and peak can also be caused by transient light, including that from kilonovae, SNe (Type Ia, Ib/c, Ic-BL, and II), superluminous SNe (SLSNe), tidal disruption events (TDEs), fast optical transients (FOTs), and the empirical subpopulations of fast blue optical transients (FBOTs), where  $g - r \lesssim -0.2$  following A. Y. Q. Ho et al. 2023) and luminous FBOTs (LFBOTs), which we define as FBOTs with  $M_{\text{peak}} < -20.5$  in rest-frame  $g$ . We compare GRB 210704A to these transients in Fig. 11, where we plot the peak absolute magnitude versus the duration above half-maximum flux in the rest frame.

The excess emission in GRB 210704A is much more luminous than prototypical kilonova AT2017gfo and can therefore not be explained by the typical SGRB progenitor scenario. A brighter kilonova may be possible if it is powered by a magnetar. We discuss this scenario further in Section 4.4.4, where we perform modelling.

The luminosity and duration of GRB 210704A’s excess are also inconsistent with a typical SN Ic-BL that is commonly associated with LGRBs (Fig. 11). Additionally, GRB 210704A’s excess rises on a shorter time-scale than SNe Ic-BL (upper left panel of Fig. 12). We can exclude other standard core-collapse SN (Type Ib/Ic/II) or thermonuclear (Ia) SN progenitors for the same brightness and temporal reasons (Fig. 11). SLSNe and TDEs match GRB 210704A in brightness, but evolve on longer time-scales.

GRB 210704A’s excess emission is more luminous and more rapid than most FBOTs (Fig. 11 and second panel of Fig. 12). It is also brighter and redder than prototypical LFBOT AT2018cow (upper right panel of Fig. 12). However, we note that the colour may not be as important given the similarities between non-blue FOT AT2020bot (upper left black square in Fig. 11) and the blue LFBOT population. The GRB’s emission is on the bright end of



**Figure 11.** Peak absolute magnitude versus the rest-frame duration above half the peak flux, using the observed peak. We include kilonova AT2017gfo (rest-frame  $g$ ; V. A. Villar et al. 2017), SNe (rest-frame  $g/r$ ; D. A. Perley et al. 2020), SLSNe and TDEs (rest-frame  $u/g/r$ ; D. A. Perley et al. 2020), FOTs (rest-frame  $g/r$ ; A. Y. Q. Ho et al. 2023), and FBOTs and LFBOTs (band closest to rest-frame  $g$ ; A. Y. Q. Ho et al. 2023; M. Pursiainen et al. 2025). The LFBOTs are empirically selected as FBOTs with  $M_{\text{peak}} < -20.5$  mag. We also plot EP240414a (rest-frame  $g$ ), EP241021a (rest-frame  $g$ ), and GRB 210704A (rest-frame  $r$ ), for which we calculated the duration (Table 4). Magnitudes were corrected for Galactic extinction and in the case of iPTF15ul also for host extinction (D. A. Perley et al. 2020).

the population of LFBOTs (Fig. 11), comparable in brightness to most luminous LFBOT known to date – AT2024wpp (lower left panel of Fig. 12).

Luminous and rapidly brightening optical counterparts have been observed for some fast X-ray transients (FXTs). The *Einstein Probe* FXT EP240414a (J. S. Bright et al. 2025; S. Srivastav et al. 2025; H. Sun et al. 2025; J. N. D. Van Dalen et al. 2025) is a prime example. Its light curve consists of an early decay, a rebrightening episode that peaks at 2.9 d in the rest frame ( $z = 0.401$ ), and a late-time fainter rebrightening that starts after 7 rest-frame days (Fig. 12). The brightest (2.9 d) peak resembles the excess in GRB 210704A in peak time and colour (fifth panel of Fig. 12), although it differs in peak magnitude and in peak sharpness (Fig. 11). EP240414a has a massive star origin, as late-time spectroscopy reveals an SN Ic-BL (J. N. D. Van Dalen et al. 2025). The radio emission strongly resembles a moderately relativistic afterglow typical for collapsar LGRBs (J. S. Bright et al. 2025), despite no gamma-ray counterpart having been detected. A possible gamma-ray counterpart of EP240414a is constrained to  $L_{\text{iso}} < 10^{51}$  erg  $s^{-1}$  (J. S. Bright et al. 2025), which could suggest that EP240414a is a low-luminosity GRB event. This is in stark contrast to GRB 210704A, for which the LAT detection indicates a high bulk Lorentz factor. Motivated by EP240414a’s soft X-ray spectrum (peaking  $< 1.3$  keV), its spectral features, and its large offset from its peculiar host galaxy, H. Sun et al. (2025) propose a stripped-envelope Wolf–Rayet star progenitor that launches a weaker jet than typical for LGRB progenitors, potentially due to

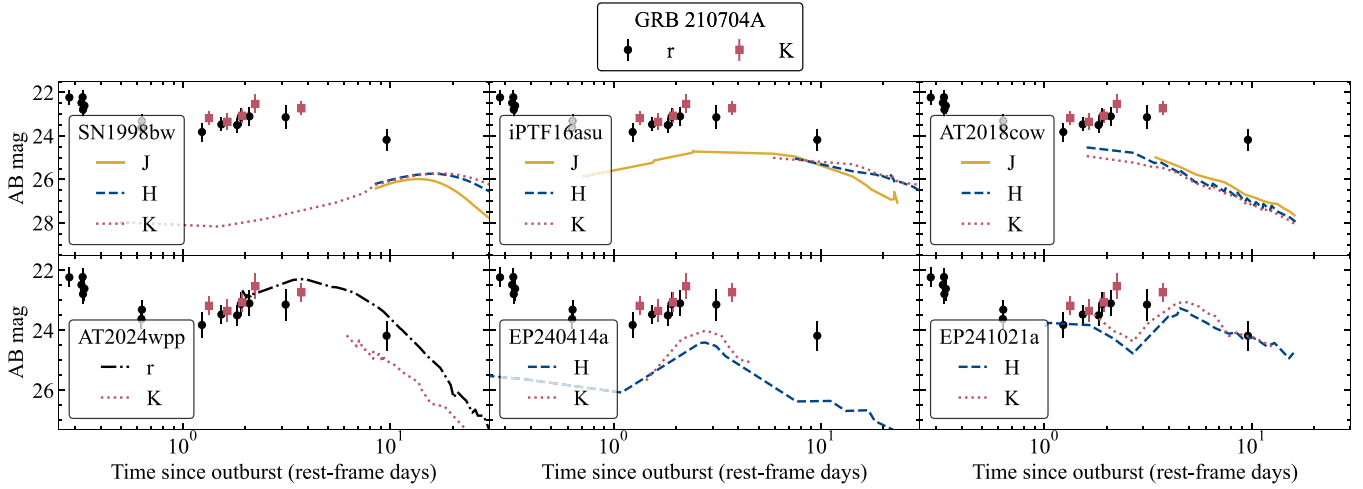
a smaller core angular momentum. For the main optical peak in EP240414a’s light curve, S. Srivastav et al. (2025) suggest a refreshed shock scenario. However, just like for GRB 210704A, the X-ray light curve of EP240414a declines and the spectral index  $\beta_{\text{ox}}$  steepens during the main optical peak. J. N. D. Van Dalen et al. (2025) argue that this decoupling of the X-ray and optical light curves disfavors an afterglow origin. They propose a low-luminosity collapsar GRB scenario with early cocoon emission, a bright peak due to SN–CSM interaction, and the late peak corresponding to SN emission. We explore both refreshed shocks and SN–CSM interaction as possible origins of GRB 210704A’s excess in Section 4.4.

Another optically luminous and rapid FXT is EP241021a (M. Busmann et al. 2025; G. Gianfagna et al. 2025; X. Shu et al. 2025; G.-L. Wu et al. 2025; M. Yadav et al. 2025; Quirola-Vásquez et al. 2026). It is not detected in gamma-rays, but the limits on the gamma-ray emission are shallow (M. Busmann et al. 2025). EP241021a’s optical light curve exhibits an initial afterglow-like decay, followed by a rapid rebrightening peak at 4.4 rest-frame days ( $z = 0.748$ ) and a shallower peak at 11 rest-frame days (lower right panel of Fig. 12). The late-time peak can be explained by an emerging SN, implying a collapsar origin for EP241021a (G. Gianfagna et al. 2025; J. Quirola-Vásquez et al. 2026). The radio afterglow points to an at least mildly relativistic outflow, connecting EP241021a to GRB-like explosions or relativistic TDEs (M. Yadav et al. 2025). The brightest peak of EP241021a resembles the peak of GRB 210704A in colour, magnitude jump, and peak magnitude (Fig. 12) as well as in peak duration (Fig. 11), although GRB 210704A peaks earlier. The X-ray light curve also behaves differently, with that of EP241021a tracking the optical rebrightening. M. Busmann et al. (2025) favour the refreshed shock scenario for the non-thermal brightest peak in EP241021a. However, J. Quirola-Vásquez et al. (2026) argue that the rise time of the peak is shorter than expected for a refreshed shock and that the fast rebrightening is extremely difficult to reconcile with any interpretation. X. Shu et al. (2025) agree that the brightest peak in EP241021a cannot be well explained by existing models, including SN shock breakout, a merger-triggered magnetar, a highly structured jet or a repeating TDE.

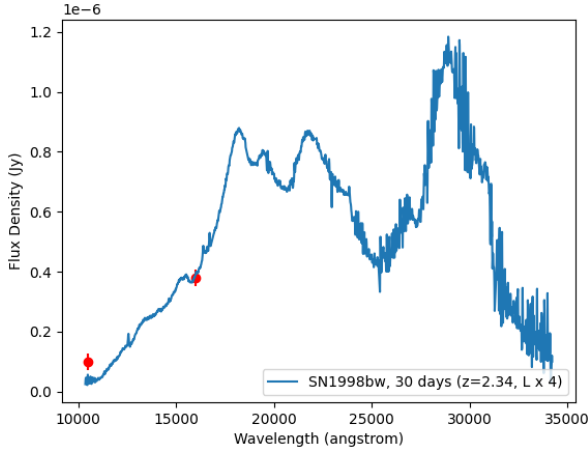
In any case, the empirical similarity of GRB 210704A to these recent *Einstein Probe* transients is notable, in particular since those systems were both much closer than GRB 210704A, but had no associated  $\gamma$ -ray emission. While similarity in emission does not necessarily imply a causal connection, it is none the less interesting to consider this difference should such a connection exist. In particular, the powerful jet in FXTs could be absent because it is not produced (e.g. because of jet launch conditions), because it is choked by heavy baryon loading in the progenitor star, or because of viewing angle effects.

### 4.3 Possible late-time supernova

As stated in Section 3.2, the morphology of the underlying source in the late-time *HST* data is characterized by a compact emission knot on top of an extended component (right panel of Fig. 5). An investigation of the emission colour reveals a red source in both *HST* epochs that yields an even redder colour for smaller apertures (from F105W – F160W =  $1.0 \pm 0.1$  in a 0.42-arcsec (6-pixel) aperture to F105W – F160W =  $1.5 \pm 0.1$  in a 0.14-arcsec aperture). This is unlikely to be caused by extinction, as F606W – F105W is blue. In the absence of an exceptionally strong Balmer line, this could indicate the presence of a red transient on top of



**Figure 12.** Light curves in the observer frame, comparing GRB 210704A to prototypical LGRB with SN Ic-BL: GRB 980425/SN1998bw (F. Patat et al. 2001), FBOT iPTF16asu, which is associated with an SN Ic-BL (L. Whitesides et al. 2017), prototypical LFBOT AT2018cow (S. J. Prentice et al. 2018), the brightest LFBOT to date: AT2024wpp (N. LeBaron et al. 2026), EP240414a (J. N. D. Van Dalen et al. 2025), and EP241021a (M. Busmann et al. 2025; J. Quirola-Vásquez et al. 2026). All transients were converted to the  $z = 2.34$  frame.



**Figure 13.** The spectrum of SN1998bw – a prototypical SN Ic-BL – (graph) taken 30 rest-frame days after its associated GRB (T. J. Galama et al. 1998; F. Patat et al. 2001), redshifted using  $z = 2.34$  and shifted to four times its luminosity to roughly match the *HST* IR detections of GRB 210704A (data points).

a galaxy. Assuming  $z = 2.34$ , the *HST* epochs were taken 32 and 58 d after the GRB in the rest frame. This is late, but not unheard of, for an SN associated with a GRB to be detected (S. E. Woosley, T. Sukhbold & D. N. Kasen 2021).

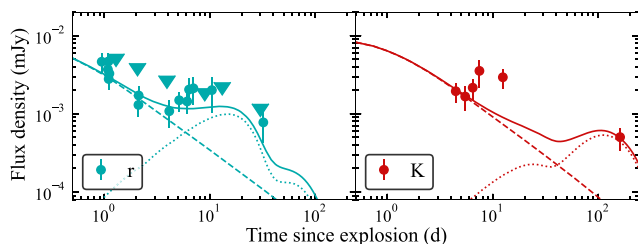
Fig. 13 compares the IR *HST* detections to a spectrum of a typical Type Ic-BL SN associated with a GRB: SN1998bw. The colour of the *HST* source is consistent with that of an SN, but the brightness of SN1998bw must be increased by a factor of 4 to align with our data. Accordingly, the transient would have an absolute magnitude of  $M_B = -20$  mag, at 30 d after the GRB in its rest frame. That is brighter than what is typically observed in Type Ic SNe (Fig. 11; M. M. Kasliwal 2012). However, we note that the underlying galaxy likely contributes to the total brightness. We further investigate the SN scenario in our modelling (Section 4.4).

GRB 241105A (Dimple et al. 2025;  $z = 2.681$ ) shares several characteristics with GRB 210704A. It exhibits a bright short ini-

tial spike followed by weaker emission up to 64 s. Although no accompanying SN was detected, *James Webb Space Telescope* observations reveal host-galaxy properties that are more typical of the LGRB population (active star formation and a low metallicity). Combined with the small sub-kpc offset from the host and afterglow modelling that requires a high-density CSM, a collapsar origin for GRB 241105A is plausible. However, we note that the prolonged emission in GRB 241105A is spectrally harder than its initial spike, which is atypical for EE-GRBs (e.g. Y. Kaneko et al. 2015). In this respect, GRB 210704A more closely resembles the canonical EE-GRB population. Detecting an SN associated with GRB 210704A would challenge the standard picture where EE-GRBs originating solely from compact object mergers. New *HST* imaging would be able to confirm whether an SN signature was indeed present in the late-time epochs.

#### 4.4 Light-curve modelling with REDBACK

We have shown that the excess emission of GRB 210704A is not easily matched to the emission observed in other transients, although substantial similarities can be found to some classes. In this section, we attempt to model the light curve of GRB 210704A with combined afterglow, interaction, and/or transient models. We adopt a joint fitting approach, rather than fitting individual model components or parameters independently, in order to avoid introducing significant biases in the inferred posterior distributions (W. F. Wallace & N. Sarin 2025). For the joint fitting, we use Bayesian inference software package REDBACK (N. Sarin et al. 2024, 2025) and the NESSAI sampler (M. J. Williams, J. Veitch & C. Messenger 2021, 2023; M. J. Williams, J. Veitch & C. Chapman-Bird 2025) wrapped with BILBY (G. Ashton et al. 2019; C. Talbot et al. 2025). We use a standard Gaussian likelihood and the default model priors in REDBACK, except for the redshift, which we set to  $z = 2.34$ . We include the late-time *HST* and Gemini photometry in the modelling, as the late-time data may include an SN component (Section 4.3).



**Figure 14.** Top-hat afterglow model (G. Ryan et al. 2020) combined with an SN–CSM interaction model (B. Margalit 2022) and an SN model (W. D. Arnett 1982), fitted to the  $r$ - (left panel) and  $K$ -band (right panel) data of GRB 210704A (solid graph). The dashed and dotted graphs represent the afterglow model and the combined CSM shock and SN model, respectively. The SN–CSM interaction and SN models share a common photosphere and diffusion description and are therefore plotted as one graph, where the early-time peak is due to the CSM shock and the late-time peak is due to the SN. The model fits correspond to the maximum posterior (prior  $\times$  likelihood).

#### 4.4.1 SN–CSM interaction

Motivated by the similarities with EP240414a, we first use a combined model of a top-hat afterglow, CSM shock breakout, and an SN. In particular, we use the semi-analytical top-hat model from AFTERGLOWPY (G. Ryan et al. 2020). This model assumes a decelerating jet in a homogeneous medium and approximates the jet as a single-shell (H. Eerten, W. Zhang & A. MacFadyen 2010; H. Eerten 2018) to compute light curves. Relativistic beaming and (conical) jet spreading are taken into account. We also include inverse Compton scattering in an attempt to simultaneously explain the high-energy LAT emission. For the CSM interaction, we use the spherically symmetric one-zone model from B. Margalit (2022). The model assumes a one-zone shell of ejecta, interacting with a CSM shell of thickness  $\Delta R_{\text{shell}}$  and mass  $M_{\text{CSM}}$  with a constant density (top-hat) profile, located at distance  $R_{\text{shell}}$  from the progenitor. The CSM shell is assumed to expand homologously, starting at the time of shock breakout (when photons are first able to escape the shocked CSM). The model explicitly solves the radiative diffusion equation to capture energy transport and losses. To model the SN emission produced by the radioactive decay of  $^{56}\text{Ni}$ , we use the well-established analytical framework of W. D. Arnett (1982). We note that the models we use are highly simplified, e.g. assuming spherical symmetry and a single zone. None the less, these models have proven to be successful in reproducing observed light curve features (e.g. J. N. D. Van Dalen et al. 2025).

The combined model fit is shown in Figs 14 and 15, where the former highlights the contributions of the different models and the latter shows the 90 per cent credible intervals of the combined model fitted to all available data. The combined model fails to explain all the data. Although the excess emission in  $r$  could be consistent with SN–CSM interaction, the model cannot account for the contemporaneous excess in  $K$  or  $z$ . We also note that the afterglow model, despite including inverse Compton scattering, struggles to explain the LAT emission of GRB 210704A.

The posterior distribution is shown in Fig. A1. The afterglow posterior is not well constrained, but generally implies a highly energetic jet with a relatively large core angle, which is observed on-axis. The jet angle may be overestimated as the modelling assumes a top-hat jet rather than a structured jet. The initial Lorentz factor is unconstrained by the modelling, which is ex-

pected as there are no early-time X-ray/optical/IR observations. We note that the CSM interaction model produces a high ejecta velocity and high CSM mass, which is in stark contrast to the prior distributions which favour smaller values. The CSM parameters are likely overestimated as a result of the simplifications made in the modelling, such as the one-zone assumption. The same is true for the unusually high nickel fraction, mass, and velocity found by the simple one-zone SN model. Including additional physics could result in better parameter estimates. For example, including nickel mixing could yield a lower nickel fraction and ejecta velocity. Although the modelling produces a low opacity to gamma-rays and a low temperature floor, this is in line with the prior distributions and therefore not unexpected.

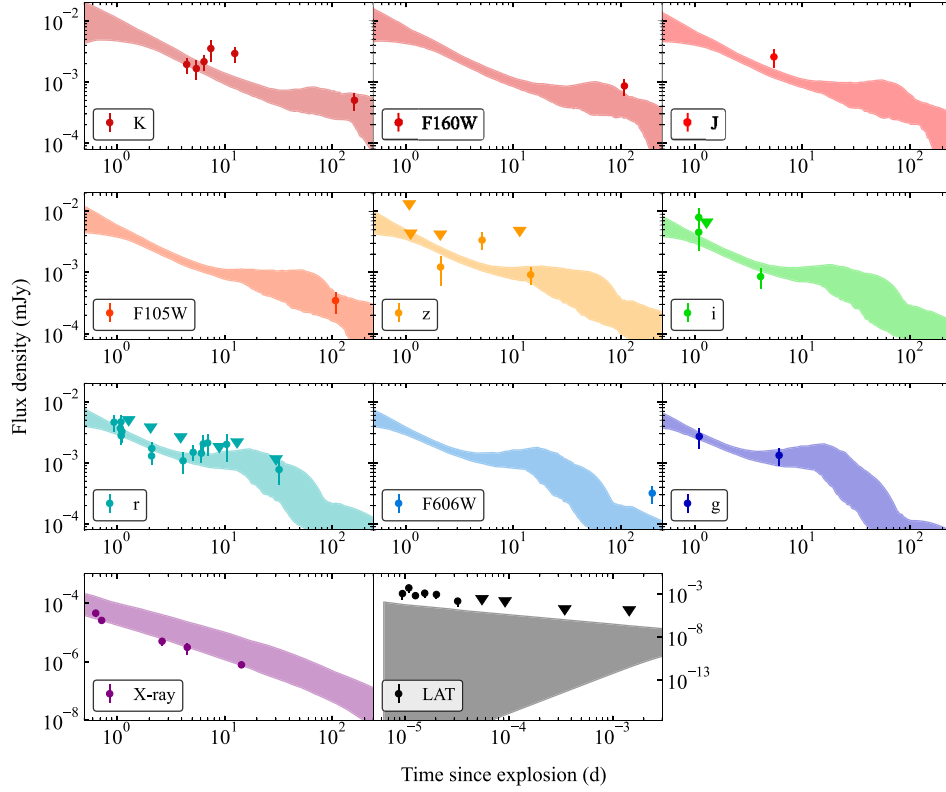
#### 4.4.2 Refreshed Afterglow

The refreshed shock afterglow model was proposed for EP240414a (S. Srivastav et al. 2025) and EP241021a (M. Busmann et al. 2025), both of which resemble GRB 210704A in many ways. We therefore investigate the refreshed shock scenario in more detail. For hydrodynamically accelerated GRB ejecta, K. Ioka, S. Kobayashi & B. Zhang (2005) calculate that refreshed shocks can only produce bumps with  $t_{1/2,\text{rise}}/t_{\text{peak}} \geq 0.25$ . For GRB 210704A, the observed ratio is  $\approx 0.4 \pm 0.2$  for  $r$  and  $\approx 0.2 \pm 0.1$  for  $K$ , making the refreshed shock scenario a possibility. We fit a combined model of a refreshed top-hat afterglow and an SN to the light curve of GRB 210704A.

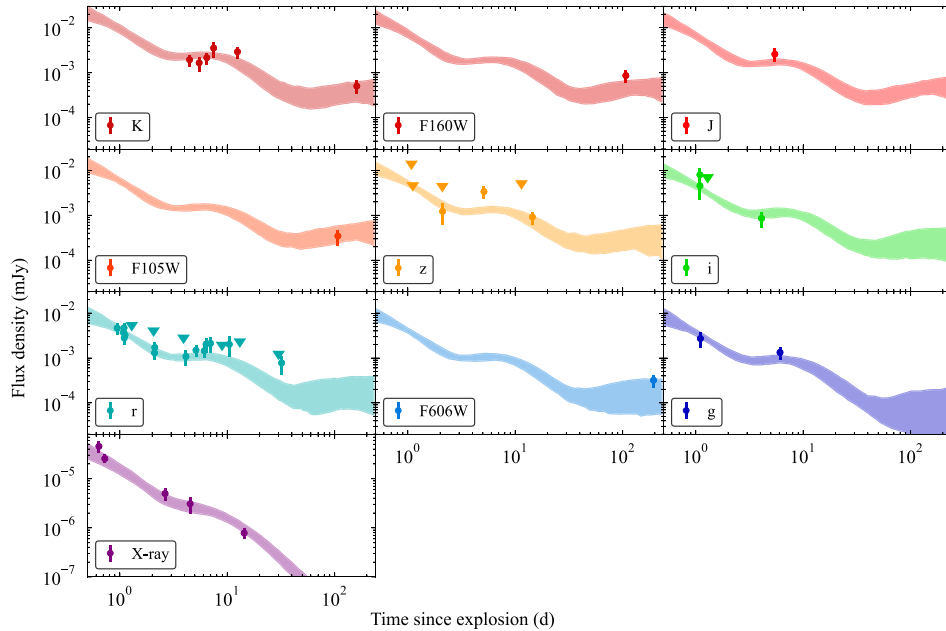
For the SN model, we again use the analytical model from W. D. Arnett (1982). For the refreshed top-hat afterglow, we use the model from G. P. Lamb et al. (2019) and G. P. Lamb et al. (2020), see also N. Sarin et al. (2024), where the model is included in REDBACK. This model assumes that the refreshed afterglow is the result of energy injection due to a collision between a slower catching shell and the decelerating impulsive shell. The resultant merged shell is the sum of the two shell masses. The energy injection is modelled as a mild collision, i.e. no secondary shock is produced within the hot impulsive shell at collision and the two shells stick together (see B. Zhang & P. Mészáros 2002 for details). The afterglow emission model includes synchrotron self-absorption and pre-deceleration physics, where the jet’s coasting phase is included before the deceleration time. The model includes a jet spreading description that follows either of the two cases in J. Granot & T. Piran (2012) ( $\alpha = 1$  case is used). However, as this model does not include inverse Compton scattering, we exclude the LAT data from the modelling here.

The combined model fit is shown in Figs 16 and 17, where the former shows the 90 per cent credible intervals of the combined model fitted to all available data and the latter highlights the contributions of the different models. While the X-ray data do not require a refreshed shock, the refreshed-afterglow model provides an adequate description of them (Fig. 16). The late-time steepening of the X-ray light curve is consistent with a cooling break passing through the X-ray band, which, following the closure relations, would result in a slope of  $\alpha = -1.5$  (using electron index  $p = 2.6$  as determined earlier and assuming a uniform medium and the slow-cooling regime).

The posterior distribution is shown in Fig. A2. Similar to what was discussed in Section 4.4.1, the afterglow modelling is unable to constrain the initial Lorentz factor and produces a large core angle, which are likely the result of not having early-time



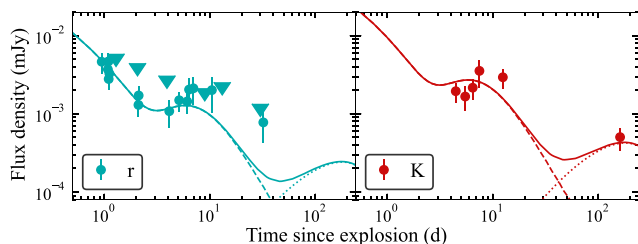
**Figure 15.** Top-hat afterglow model (G. Ryan et al. 2020) combined with an SN–CSM interaction model (B. Margalit 2022) and an SN model (W. D. Arnett 1982), fitted to the light curve of GRB 210704A with REDBACK using 1000 live points. The afterglow model includes inverse Compton scattering and jet spreading. The shaded areas are the 90 per cent credible intervals.



**Figure 16.** Refreshed top-hat afterglow model (G. P. Lamb et al. 2019; G. P. Lamb, A. J. Levan & N. R. Tanvir 2020) combined with an SN model (W. D. Arnett 1982), fitted to the light curve of GRB 210704A with REDBACK using 500 live points. The shaded areas are the 90 per cent credible intervals.

observations and of the top-hat assumption in the modelling, respectively. We note that the light curve of GRB 210704A can only be explained by a strong refreshed shock (Fig. A2): it requires a dense CSM (number density  $n_{\text{ism}} \approx 50 \text{ cm}^{-3}$ ), a large Lorentz

factor of the shell at the onset of energy injection  $\Gamma_1 \approx 4.8$ , a kinetic energy increase by a factor of  $\approx 18$ , a relatively high energy injection index ( $s \approx 9$  and consistent with a uniform Lorentz factor throughout the catching shell), and a high electron energy



**Figure 17.** Refreshed top-hat afterglow model (G. P. Lamb et al. 2019; G. P. Lamb et al. 2020) combined with an SN model (W. D. Arnett 1982), fitted to the  $r$ - (left panel) and  $K$ -band (right panel) data of GRB 210704A (solid graph). The dashed and dotted graphs represent the refreshed afterglow and the SN model, respectively. The model fits correspond to the maximum posterior (prior  $\times$  likelihood).

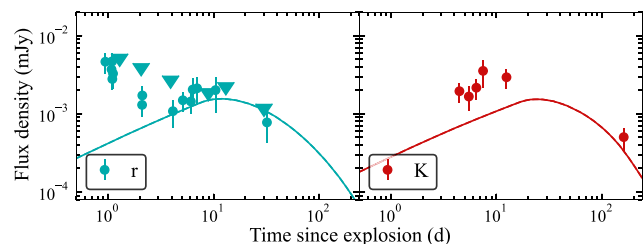
fraction  $\epsilon_e \approx 0.5$ . The model thus requires the trailing ejecta shell, which catches up with the earlier ejected shell to cause the refreshed shock, to be highly energetic. Such a strong shock can explain the optical/IR excess emission around  $\approx 5$ –15 d reasonably well, although the model struggles to explain the  $z$ -band peak (Fig. 16).

Additionally, the modelling shows that most of the late-time data can be decently explained as SN emission. The combined model struggles with the  $r$ -band detection at 32 d. However, the SN model used here is a simple one-zone model (W. D. Arnett 1982) that does not include nickel mixing. When  $^{56}\text{Ni}$  is mixed with the outer layers of the SN ejecta, the energy produced by the radioactive decay of  $^{56}\text{Ni}$  dissipates more easily through the ejecta, resulting in earlier SN emission (e.g. M. C. Bersten et al. 2012; J. C. Rastinejad et al. 2025). An earlier rise in the SN light curve could explain GRB 210704A’s  $r$ -band detection at 32 d, as well as better explain the detection in F160W (Fig. 16). The elevated nickel fraction, ejecta mass, and ejecta velocity are again likely an artefact of the simple SN model, where e.g. nickel mixing is excluded and one zone is assumed.

#### 4.4.3 Shock cooling

We also attempt to fit GRB 210704A’s light curve with a combined top-hat afterglow, shock cooling, and SN model. As in Section 4.4.1, we use the top-hat afterglow model from AFTERGLOWPY (G. Ryan et al. 2020), including jet spreading and inverse Compton scattering. For the SN model, we use the analytical model from W. D. Arnett (1982) as before. For the shock cooling emission, we use the analytical model from A. L. Piro et al. (2021). In this model, a shock wave deposits energy  $E_{\text{en}}$  into extended material of mass  $m_{\text{en}}$  and radius  $R_{\text{en}}$ , causing the material to expand homologously. The model only considers the homologously expanding phase and assumes a constant electron scattering opacity (motivated by the hot ejecta temperatures). The expanding ejecta are considered to have a two-component profile (R. A. Chevalier & N. Soker 1989), where the outer component has a strong velocity gradient and the inner ejecta have a more modest velocity gradient. The power-law slopes of the density profiles are parametrized by  $nn$  and  $\Delta$  for the outer and inner ejecta, respectively. This is a common assumption for density profiles in all models involving a massive star progenitor.

The combined model fit is shown in Figs 18 and 19, where the former highlights the contributions of the different models and the latter shows the 90 per cent credible intervals of the combined



**Figure 18.** Top-hat afterglow model (G. Ryan et al. 2020) combined with a shock cooling model (A. L. Piro, A. Haynie & Y. Yao 2021) and an SN model (W. D. Arnett 1982), fitted to the  $r$ - (left panel) and  $K$ -band (right panel) data of GRB 210704A (solid graph). The model fit correspond to the maximum posterior (prior  $\times$  likelihood). The shock cooling and SN contributions are negligible in the maximum posterior fit.

model fitted to all available data. Although the data largely fall in the 90 per cent credible interval of the combined model, the maximum posterior curve is a poor fit to the data (Fig. 18).

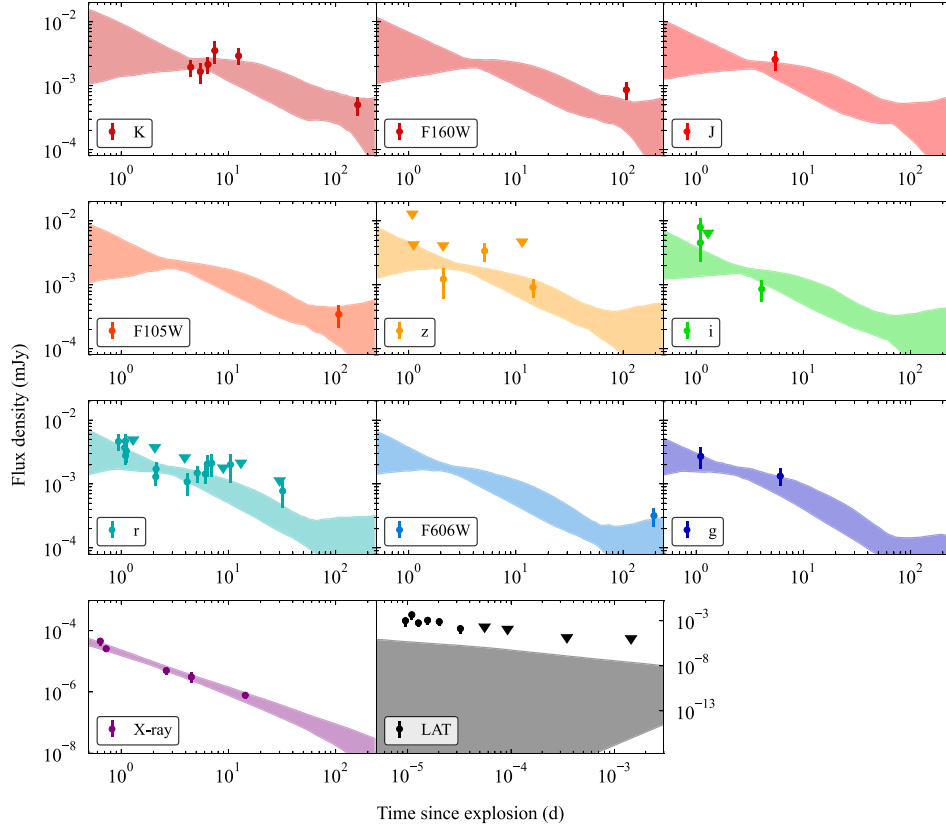
The posterior distribution is shown in Fig. A3. As in our previous modelling, the large jet core angle and nickel fraction are likely overestimated due to the model assumptions and missing physics. We note that the posterior of the shock cooling model is very poorly constrained. Combined with the poor maximum posterior fit, we therefore disfavour the combined top-hat afterglow, shock cooling, and SN model.

#### 4.4.4 Alternative models

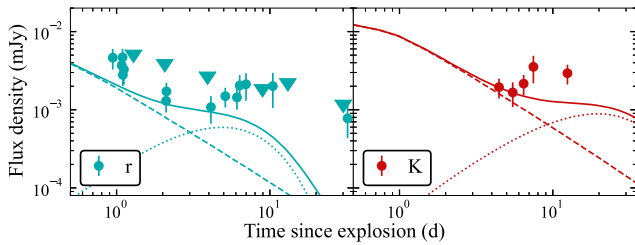
Alternative models for light curve bumps include the patchy shell model (P. Mészáros, M. J. Rees & R. A. M. J. Wijers 1998; P. Kumar & T. Piran 2000), a density bump in the CSM (X. Wang & A. Loeb 2000; Z. G. Dai & T. Lu 2002; D. Lazzati et al. 2002; E. Nakar et al. 2003) or a magnetar-driven transient. The patchy shell model describes a jet where the energy varies randomly across its head, resulting in ‘hot spots’ or ‘sub-jets’. The excess in GRB 210704A violates the model requirement of  $t_{1/2,\text{rise}} > t_{\text{peak}}$  (K. Ioka et al. 2005). The density bump scenario is also implausible, since GRB 210704A violates the possible maximum amplitude of the rebrightening  $\Delta F_v/F_v \leq 1.6 t_{1/2,\text{rise}}/t_{\text{peak}}$  assuming a typical on-axis afterglow (K. Ioka et al. 2005), with  $\Delta F_v/F_v = 0.7$  for GRB 210704A in  $K$  (rest-frame  $r$ ). To investigate a possible magnetar-driven kilonova origin, we use REDBACK to fit the general magnetar-driven kilonova model from N. Sarin et al. (2022) to the data of GRB 210704A (Figs 20 and 21). Although the  $r$ -band data largely fall within the 90 per cent credible interval of the magnetar-driven kilonova model, GRB 210704A is brighter in  $K$  and  $z$  than expected for such a transient. Additionally, the maximum posterior light curve is a poor fit in both  $K$  and  $r$ .

#### 4.5 Fermi/LAT emission

Our analysis of the *Fermi* data over the first 4 s after the burst gives a hard LAT spectral index of  $-1.64 \pm 0.139$  and a significantly softer high-energy band index derived from GBM data  $\beta \approx -2.86 \pm 0.16$ . This indicates the presence of an additional, harder, spectral component at GeV energies. Our broad-band afterglow modelling (Section 4.4; based on X-ray, optical, and IR data), including inverse Compton scattering, fails to reproduce the observed LAT flux (see Figs 15 and 19). A simple extrapolation of the fitted afterglow model to GeV energies also underpredicts



**Figure 19.** Top-hat afterglow model (G. Ryan et al. 2020) combined with a shock cooling model (A. L. Piro et al. 2021) and an SN model (W. D. Arnett 1982), fitted to the light curve of GRB 210704A with REDBACK using 1000 live points. The shaded areas are the 90 per cent credible intervals.



**Figure 20.** Top-hat afterglow model (G. P. Lamb, I. Mandel & L. Resmi 2018; N. Sarin et al. 2024) combined with a general magnetar-driven kilonova model (N. Sarin et al. 2022), fitted to the *r*- (left panel) and *K*-band (right panel) data of GRB 210704A (solid graph). The dashed and dotted graphs represent the afterglow and the magnetar-driven kilonova model, respectively. The model fits correspond to the maximum posterior (prior  $\times$  likelihood).

the LAT flux. The origin of the LAT emission therefore remains unclear. A detailed investigation of the hard GeV component lies beyond the scope of this work.

#### 4.6 SED fitting caveats

We note that if an SN is present in the *HST* epochs, this will impact the accuracy of our SED fits. The *HST* and Gemini epochs that were used for the fitting would include the transient, therefore resulting in an overestimation of the brightness of the underlying galaxy. For consistency, we ran PROSPECTOR again with a fixed  $z = 2.34$  on adapted photometry, where we assumed only

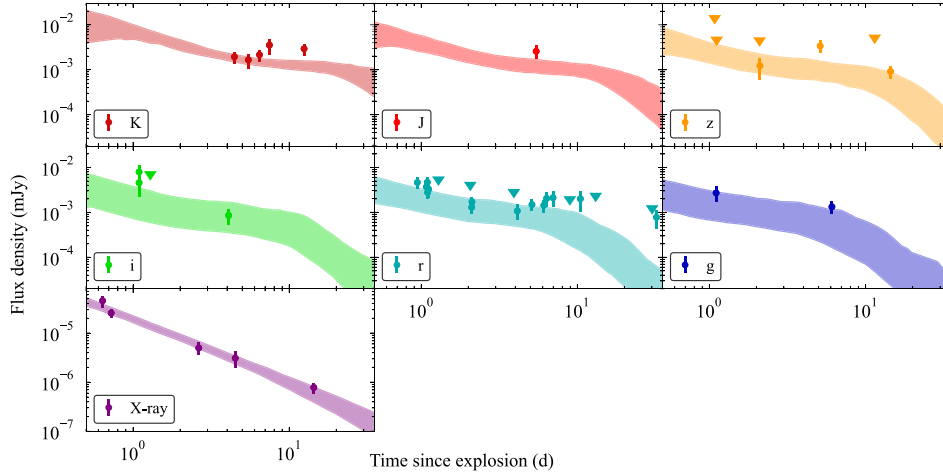
half of the flux of the late-time *HST* and Gemini data is attributed to the galaxy. The resulting galaxy parameters are consistent with the parameters that we obtained before, so the effect of a possible SN on our SED fits is small.

## 5 CONCLUSIONS

We presented a detailed multiwavelength analysis of GRB 210704A. From our low-S/N afterglow spectrum, we determined a tentative redshift of  $z = 2.34$ . Line stacking the spectrum and SED fitting the photometry of the underlying extended source corroborate this redshift, which we therefore deem to be the most likely redshift of the burst.

We consider the most likely progenitor of GRB 210704A to be a collapsar. Light-curve modelling shows potential late-time SN emission. Moreover, *HST* imaging taken 58 rest-frame days post-burst shows potential SN emission on top of the host galaxy. Additionally, SED fitting yields host galaxy properties typical for core-collapse GRB progenitors and the spectral lag of GRB 210704A, its isotropic-equivalent energy, its placement on the Amati relation, and its location on top of a galaxy all point to a core-collapse progenitor.

GRB 210704A can be classified as an EE-GRB, as its short initial pulse is followed by weaker softer prompt emission. A collapsar origin is highly unusual for EE-GRBs, which are typically linked to compact object mergers. Nevertheless, proposed mechanisms for the extended emission such as magnetar spin-down or fallback accretion still apply if a (short-lived) magnetar remnant is formed after the SN.



**Figure 21.** Top-hat afterglow model (G. P. Lamb et al. 2018; N. Sarin et al. 2024) combined with a general magnetar-driven kilonova model (N. Sarin et al. 2022), fitted to the light curve of GRB 210704A. The shaded areas are the 90 per cent credible intervals.

The light curve of GRB 210704A contains rapid highly luminous optical/IR emission that peaks around 7 d reaching  $M_r = -22$  mag. It resembles LFBOT emission, despite the LFBOT population generally not exhibiting obvious SN signatures at any epoch. Additionally, it closely resembles the bright emission peak observed in FXT EP241021a and has some similarities to the bright peak in FXT EP240414a. These similarities reinforce the notion that the same emission mechanisms could be at play for some LFBOTs, FXTs, and GRBs. Markedly, GRB 210704A has high-energy gamma-ray detections in *Fermi*/LAT, which indicates a high bulk Lorentz factor. The link between low-luminosity GRBs, FXTs, and LFBOTs has been suggested before (e.g. J. N. D. Van Dalen et al. 2025), but GRB 210704A shows that high-luminosity GRBs could also be linked to these sources.

R. L. Becerra et al. (2023) disregard a collapsar origin at  $z = 2.34$  on the basis of not being able to explain the rapid highly luminous optical/IR emission of GRB 210704A. However, our light-curve modelling, using Bayesian inference package REDBACK, shows that the excess emission could potentially originate from an energetic refreshed shock in the GRB afterglow. As refreshed shocks can also be at play in merger GRBs (e.g. G. P. Lamb et al. 2020), the connection between GRB 210704A, FXTs, and LFBOTs does not necessarily suggest similar progenitors.

## ACKNOWLEDGEMENTS

This publication is part of the Dutch Black Hole Consortium with project number NWA.1292.19.202 of the research programme NWA, which is (partly) financed by the Dutch Research Council (NWO).

JCR was supported by NASA through the NASA Hubble Fellowship grant #HST-HF2-51587.001-A awarded by the Space Telescope Science Institute, which is operated by the Association of Universities for Research in Astronomy, Inc., for NASA, under contract NAS5-26555. AR acknowledges support from INAF project *Supporto Arizona & Italia*. Dimple acknowledges support from STFC grant No. ST/Y002253/1. DBM is funded by the European Union (ERC, HEAVYMETAL, 101071865). Views and opinions expressed are, however, those of the authors only and do not necessarily reflect those of the European Union or the

European Research Council. Neither the European Union nor the granting authority can be held responsible for them. The Cosmic Dawn Center (DAWN) is funded by the Danish National Research Foundation under grant DNR140.

Based on observations obtained at the international Gemini Observatory (programme ID GN-2021B-Q-109), a programme of NOIRLab, which is managed by the Association of Universities for Research in Astronomy (AURA) under a cooperative agreement with the National Science Foundation on behalf of the Gemini Observatory partnership: the National Science Foundation (United States), National Research Council (Canada), Agencia Nacional de Investigación y Desarrollo (Chile), Ministerio de Ciencia, Tecnología e Innovación (Argentina), Ministério da Ciência, Tecnologia, Inovações e Comunicações (Brazil), and Korea Astronomy and Space Science Institute (Republic of Korea). Processed using the Gemini IRAF package and DRAGONS.

This work is partly based on data obtained with the instrument OSIRIS, built by a Consortium led by the Instituto de Astrofísica de Canarias in collaboration with the Instituto de Astronomía of the Universidad Autónoma de México. OSIRIS was funded by GRANTECAN and the National Plan of Astronomy and Astrophysics of the Spanish Government. The GTC data were obtained under programme GTCMULTIPLE2C-21A.

This work is partly based on observations made with the Nordic Optical Telescope, owned in collaboration by the University of Turku and Aarhus University, and operated jointly by Aarhus University, the University of Turku and the University of Oslo, representing Denmark, Finland and Norway, the University of Iceland and Stockholm University at the Observatorio del Roque de los Muchachos, La Palma, Spain, of the Instituto de Astrofísica de Canarias. The NOT data were obtained under programme ID 63-503.

This publication is partly based on observations made with the Javalambre Observatory (OAJ), within programme 2100193 (PI: Agüí Fernández, J. F.).

Partly based on observations made with the Italian Telescopio Nazionale Galileo (TNG) operated by the Fundación Galileo Galilei (FGG) of the Istituto Nazionale di Astrofisica (INAF) at the Observatorio del Roque de los Muchachos (La Palma, Canary Islands, Spain). The TNG data were obtained under programme A43TAC\_2.

Partly based on observations made with the William Herschel Telescope operated on the island of La Palma by the Isaac Newton Group of Telescopes in the Spanish Observatorio del Roque de los Muchachos of the Instituto de Astrofísica de Canarias (proposál QHY).

Partly based on observations collected at Centro Astronómico Hispano en Andalucía (CAHA) at Calar Alto, proposál 21B-2.2-018, operated jointly by Junta de Andalucía and Consejo Superior de Investigaciones Científicas (IAA-CSIC).

This research is based on observations made with the NASA/ESA *Hubble Space Telescope* obtained from the Space Telescope Science Institute, which is operated by the Association of Universities for Research in Astronomy, Inc., under NASA contract NAS 5-26555. These observations are associated with programme 16275.

This work is partially based on observations obtained at the LBT under programme ID IT-2021B-018. The LBT is an international collaboration of the University of Arizona, Italy (INAF: Istituto Nazionale di Astrofísica), Germany (LBTB: LBT Beteiligungsgesellschaft), The Ohio State University, representing also the University of Minnesota, the University of Virginia, and the University of Notre Dame.

Based on observations obtained with MegaPrime/MegaCam, a joint project of CFHT and CEA/DAPNIA, at the Canada–France–Hawaii Telescope (CFHT), which is operated by the National Research Council (NRC) of Canada, the Institut National des Sciences de l’Univers of the Centre National de la Recherche Scientifique (CNRS) of France, and the University of Hawaii. The observations at the Canada–France–Hawaii Telescope were performed with care and respect from the summit of Maunakea, which is a significant cultural and historic site.

This paper is based (in part) on data from the Hyper Suprime-Cam Legacy Archive (HSCLA), which is operated by the Subaru Telescope. The original data in HSCLA were collected at the Subaru Telescope and retrieved from the HSC data archive system, which is operated by the Subaru Telescope and Astronomy Data Center at National Astronomical Observatory of Japan. The Subaru Telescope is honoured and grateful for the opportunity of observing the Universe from Maunakea, which has the cultural, historical, and natural significance in Hawaii.

This paper makes use of software developed for the Vera C. Rubin Observatory. We thank the observatory for making their code available as free software at <http://dm.lsst.org>.

The Pan-STARRS1 Surveys (PS1) and the PS1 public science archive have been made possible through contributions by the Institute for Astronomy, the University of Hawaii, the Pan-STARRS Project Office, the Max-Planck Society and its participating institutes, the Max Planck Institute for Astronomy, Heidelberg and the Max Planck Institute for Extraterrestrial Physics, Garching, The Johns Hopkins University, Durham University, the University of Edinburgh, the Queen’s University Belfast, the Harvard-Smithsonian Center for Astrophysics, the Las Cumbres Observatory Global Telescope Network Incorporated, the National Central University of Taiwan, the Space Telescope Science Institute, the National Aeronautics and Space Administration under Grant No. NNX08AR22G issued through the Planetary Science Division of the NASA Science Mission Directorate, the National Science Foundation Grant No. AST-1238877, the University of Maryland, Eotvos Lorand University (ELTE), the Los Alamos National Laboratory, and the Gordon and Betty Moore Foundation.

This publication makes use of data products from the Two Micron All Sky Survey, which is a joint project of the University of Massachusetts and the Infrared Processing and Analysis Center/California Institute of Technology, funded by the National Aeronautics and Space Administration and the National Science Foundation.

Funding for the Sloan Digital Sky Survey V has been provided by the Alfred P. Sloan Foundation, the Heising-Simons Foundation, the National Science Foundation, and the Participating Institutions. SDSS acknowledges support and resources from the Center for High-Performance Computing at the University of Utah. SDSS telescopes are located at Apache Point Observatory, funded by the Astrophysical Research Consortium and operated by New Mexico State University, and at Las Campanas Observatory, operated by the Carnegie Institution for Science. The SDSS web site is [www.sdss.org](http://www.sdss.org).

SDSS is managed by the Astrophysical Research Consortium for the Participating Institutions of the SDSS Collaboration, including the Carnegie Institution for Science, Chilean National Time Allocation Committee (CNTAC) ratified researchers, Caltech, the Gotham Participation Group, Harvard University, Heidelberg University, The Flatiron Institute, The Johns Hopkins University, L’Ecole polytechnique fédérale de Lausanne (EPFL), Leibniz-Institut für Astrophysik Potsdam (AIP), Max-Planck-Institut für Astronomie (MPIA Heidelberg), Max-Planck-Institut für Extraterrestrische Physik (MPE), Nanjing University, National Astronomical Observatories of China (NAOC), New Mexico State University, The Ohio State University, Pennsylvania State University, Smithsonian Astrophysical Observatory, Space Telescope Science Institute (STScI), the Stellar Astrophysics Participation Group, Universidad Nacional Autónoma de México, University of Arizona, University of Colorado Boulder, University of Illinois at Urbana-Champaign, University of Toronto, University of Utah, University of Virginia, Yale University, and Yunnan University.

This work made use of *ASTROPY*:<sup>5</sup> a community-developed core Python package and an ecosystem of tools and resources for astronomy (Astropy Collaboration 2022; Astropy Collaboration 2024). Additionally, this work made use of *ASTROQUERY* (A. Ginsburg et al. 2019; A. Ginsburg et al. 2025), *MATPLOTLIB* (J. D. Hunter 2007; The Matplotlib Development Team 2025), *NUMPY* (C. R. Harris et al. 2020), and *PANDAS* (W. McKinney 2010; The pandas development team 2025).

## DATA AVAILABILITY

The data underlying this article are available in the article.

## REFERENCES

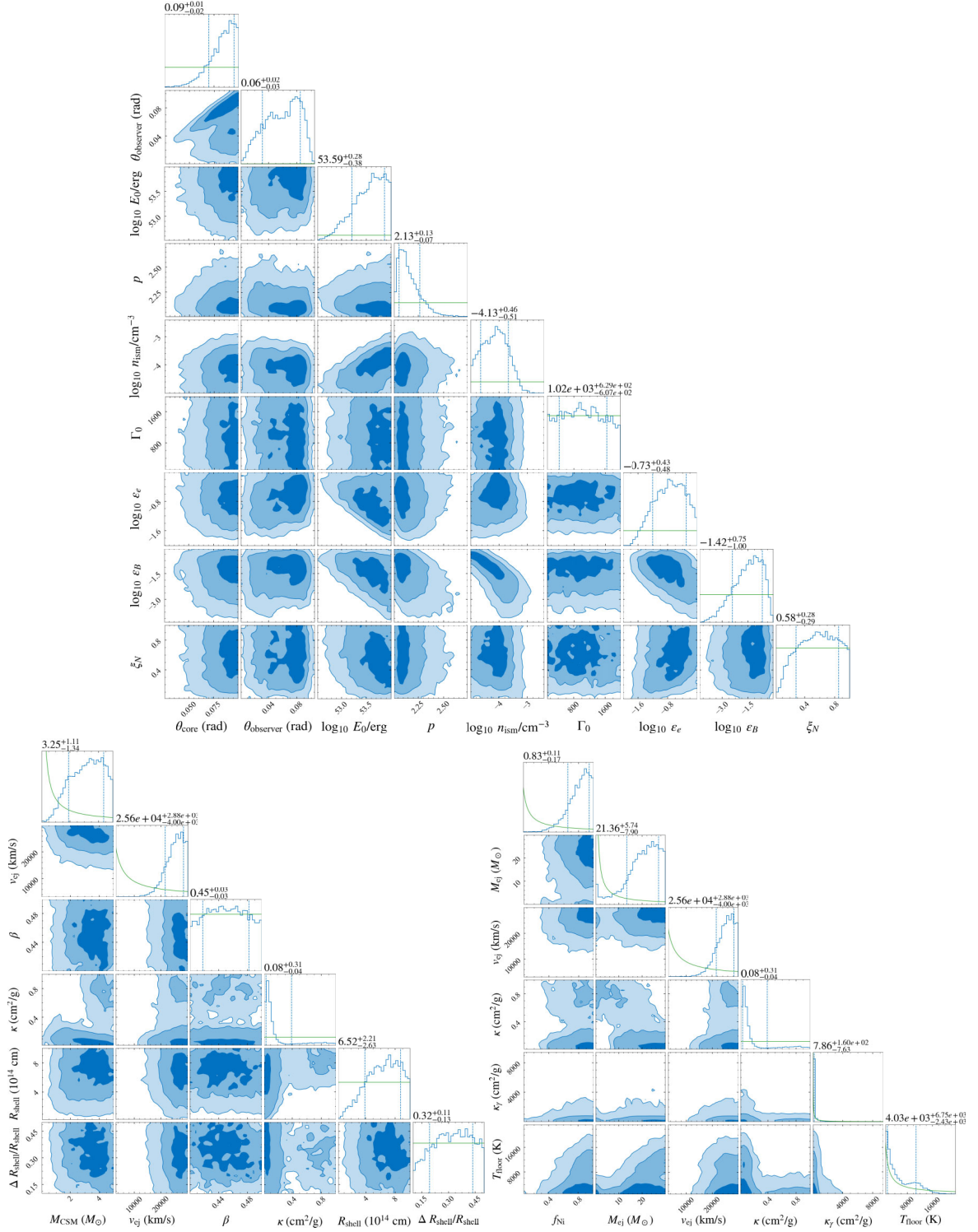
- Abazajian K. et al., 2004, *AJ*, 128, 502  
 Abbott B. P. et al., 2017, *ApJ*, 848, L12  
 Ahumada T. et al., 2021, *Nat. Astron.*, 5, 917  
 Ajello M. et al., 2019, *ApJ*, 878, 52  
 Albareti F. D. et al., 2017, *ApJS*, 233, 25  
 Anderson G. E. et al., 2025, *ApJ*, 994, 5  
 Arnett W. D., 1982, *ApJ*, 253, 785  
 Ashton G. et al., 2019, *ApJS*, 241, 27  
 Astropy Collaboration, 2024, Zenodo

<sup>5</sup><http://www.astropy.org>

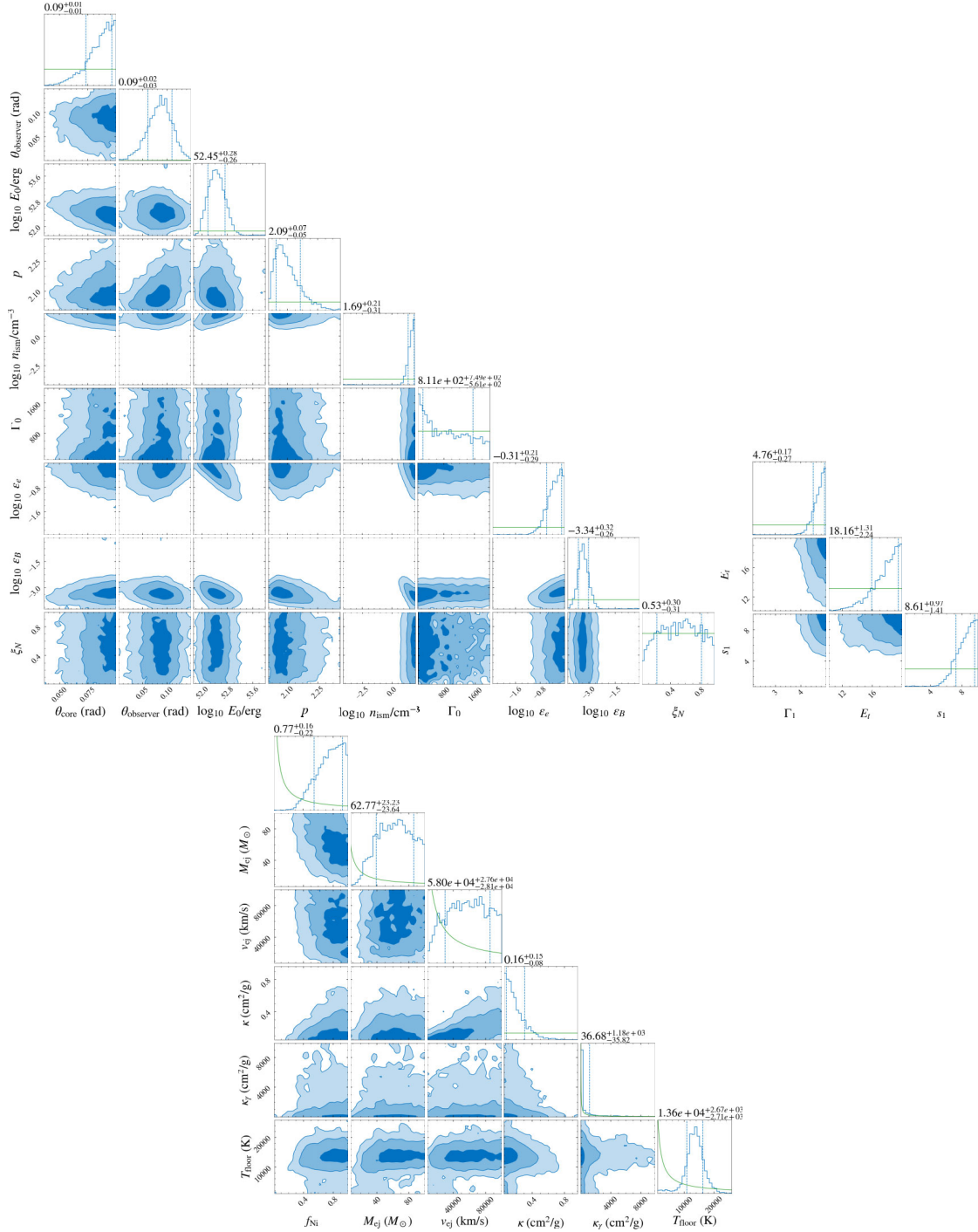
- Astropy Collaboration, 2022, *ApJ*, 935, 167
- Atwood W. B. et al., 2009, *ApJ*, 697, 1071
- Avila R. J., Hack W., Cara M., Borncamp D., Mack J., Smith L., Ubeda L., 2015, in Taylor A. R., Rosolowsky E. eds, ASP Conf. Ser. Vol. 495, Astronomical Data Analysis Software and Systems XXIV. Astron. Soc. Pac., San Francisco, p. 281
- Barkov M. V., Pozanenko A. S., 2011, *MNRAS*, 417, 2161
- Becerra R. L. et al., 2023, *MNRAS*, 522, 5204
- Becker A., 2015, Astrophysics Source Code Library, record ascl:1504.004
- Berretta A., Longo F., Axelsson M., Bissaldi E., Piron F., Arimoto M., Fermi-LAT Collaboration, 2021, GRB Coordinates Network, 30375, 1
- Bersten M. C. et al., 2012, *ApJ*, 757, 31
- Bertin E., Arnouts S., 1996, *A&AS*, 117, 393
- Bradley L. et al., 2024, Zenodo
- Breeveld A. A., Lien A. Y., Swift/UVOT Team, 2021, GRB Coordinates Network, 30389, 1
- Bright J. S. et al., 2025, *ApJ*, 981, 48
- Bucciantini N., Metzger B. D., Thompson T. A., Quataert E., 2012, *MNRAS*, 419, 1537
- Burrows D. N. et al., 2005, *Space Sci. Rev.*, 120, 165
- Busmann M. et al., 2025, *A&A*, 701, A225
- Chevalier R. A., Soker N., 1989, *ApJ*, 341, 867
- Christensen L., Fynbo J. P. U., Prochaska J. X., Thöne C. C., de Ugarte Postigo A., Jakobsson P., 2011, *ApJ*, 727, 73
- D’Ai A. et al., 2021, GRB Coordinates Network, 30379, 1
- D’Avanzo P., D’Elia V., Fiorenzano A., Padilla C., CIBO Collaboration, 2021a, GRB Coordinates Network, 30385, 1
- D’Avanzo P. et al., 2021b, GRB Coordinates Network, 30432, 1
- Dai Z. G., Lu T., 2002, *ApJ*, 565, L87
- De Pasquale M. et al., 2003, *ApJ*, 592, 1018
- De Pasquale M. et al., 2016, *MNRAS*, 455, 1027
- De Ugarte Postigo A. et al., 2021, GRB Coordinates Network, 30392, 1
- Dichiara S. et al., 2021, GRB Coordinates Network, 30383, 1
- de Ugarte Postigo A. et al., 2012, *A&A*, 548, A11
- de Ugarte Postigo A. et al., 2018, *A&A*, 620, A190
- Dimple et al., 2025, *MNRAS*, 544, 548
- Evans P. A. et al., 2007, *A&A*, 469, 379
- Evans P. A. et al., 2009, *MNRAS*, 397, 1177
- Fitzpatrick M., Placco V., Bolton A., Merino B., Ridgway S., Stanghellini L., 2025, in Jacques A., Seaman R., Gandilo N., Linder T. eds, ASP Conf. Ser. Vol. 541, Astronomical Data Analysis Software and Systems XXXIII. Astron. Soc. Pac., San Francisco, p. 461
- Flewelling H. A. et al., 2020, *ApJS*, 251, 7
- Fong W.-f. et al., 2022, *ApJ*, 940, 56
- Fraser M., 2020, *R. Soc. Open Sci.*, 7, 200467
- Fruchter A. S. et al., 2006, *Nature*, 441, 463
- Galama T. J. et al., 1998, *Nature*, 395, 670
- Gargiulo A., Fumana M., Bisogni S., Franzetti P., Cassarà L. P., Garilli B., Scodreggio M., Vietri G., 2022, *MNRAS*, 514, 2902
- Gehrels N. et al., 2006, *Nature*, 444, 1044
- Ghirlanda G., Ghisellini G., Nava L., 2010, *A&A*, 510, L7
- Gianfagna G. et al., 2025, *A&A*, 703, A92
- Ginsburg A. et al., 2019, *AJ*, 157, 98
- Ginsburg A. et al., 2025, Zenodo
- Goldstein A. et al., 2017, *ApJ*, 848, L14
- Gompertz B. P., Levan A. J., Tanvir N. R., 2020, *ApJ*, 895, 58
- Granot J., Piran T., 2012, *MNRAS*, 421, 570
- Green G. M. et al., 2015, *ApJ*, 810, 25
- Greiner J. et al., 2013, *A&A*, 560, A70
- Gruber D. et al., 2014, *ApJS*, 211, 12
- Harris C. R. et al., 2020, *Nature*, 585, 357
- Hjorth J. et al., 2003, *Nature*, 423, 847
- Ho A. Y. Q. et al., 2023, *ApJ*, 949, 120
- Hunter J. D., 2007, *Comput. Sci. Eng.*, 9, 90
- Ioka K., Kobayashi S., Zhang B., 2005, *ApJ*, 631, 429
- Jin Z.-P., Li X., Cano Z., Covino S., Fan Y.-Z., Wei D.-M., 2015, *ApJ*, 811, L22
- Johnson B. D., Leja J., Conroy C., Speagle J. S., 2021, *ApJS*, 254, 22
- Kaneko Y., Bostancı Z. F., Göğüş E., Lin L., 2015, *MNRAS*, 452, 824
- Kann D. A. et al., 2011, *ApJ*, 734, 96
- Kann D. A. et al., 2018, *A&A*, 617, A122
- Kann D. A., de Ugarte Postigo A., Thoene C., Blazek M., Agüí Fernández J. F., Martín-Fernández P., 2021a, GRB Coordinates Network, 30391, 1
- Kann D. A., de Ugarte Postigo A., Thoene C., Blazek M., Agüí Fernández J. F., Maicas N., Lamadrid J. L., 2021b, GRB Coordinates Network, 30401, 1
- Kann D. A., Izzo L., Galindo Guil F. J., Kasikov A., 2021c, GRB Coordinates Network, 30443, 1
- Kasliwal M. M., 2012, *Publ. Astron. Soc. Aust.*, 29, 482
- Kim V., Pozanenko A., Krugov M., Belkin S., Pankov N., GRB IKI FuN, 2021, GRB Coordinates Network, 30384, 1
- Kouveliotou C., Meegan C. A., Fishman G. J., Bhat N. P., Briggs M. S., Koshut T. M., Paciesas W. S., Pendleton G. N., 1993, *ApJ*, 413, L101
- Kumar P., Piran T., 2000, *ApJ*, 535, 152
- Labrie K. et al., 2023, *Res. Notes Am. Astron. Soc.*, 7, 214
- Lamb G. P., Mandel I., Resmi L., 2018, *MNRAS*, 481, 2581
- Lamb G. P. et al., 2019, *ApJ*, 883, 48
- Lamb G. P., Levan A. J., Tanvir N. R., 2020, *ApJ*, 899, 105
- Lang D., Hogg D. W., Mierle K., Blanton M., Roweis S., 2010, *AJ*, 139, 1782
- Lazzati D., Rossi E., Covino S., Ghisellini G., Malesani D., 2002, *A&A*, 396, L5
- LeBaron N. et al. 2026, *ApJ*, 997, L10
- Leja J., Johnson B. D., Conroy C., van Dokkum P. G., Byler N., 2017, *ApJ*, 837, 170
- Levan A., Crowther P., de Grijs R., Langer N., Xu D., Yoon S.-C., 2016, *Space Sci. Rev.*, 202, 33
- Levan A. J., Campana S., Kann D. A., D’Avanzo P., 2021, GRB Coordinates Network, 30381, 1
- Levan A. J. et al., 2023, *Nat. Astron.*, 7, 976
- Levan A. J. et al., 2024, *Nature*, 626, 737
- Malacaria C., Meegan C., Fermi GBM Team, 2021, GRB Coordinates Network, 30380, 1
- Margalit B., 2022, *ApJ*, 933, 238
- McKinney W., 2010, in van der Walt S., Millman J. eds, Proceedings of the 9th Python in Science Conference. SciPy, Austin, p.56
- Meegan C. et al., 2009, *ApJ*, 702, 791
- Mészáros P., Rees M. J., Wijers R. A. M. J., 1998, *ApJ*, 499, 301
- Metzger B. D., 2019, *Living Rev. Relativ.*, 23, 1
- Metzger B. D., Quataert E., Thompson T. A., 2008, *MNRAS*, 385, 1455
- Metzger B. D., Arcones A., Quataert E., Martínez-Pinedo G., 2010, *MNRAS*, 402, 2771
- Minaev P., Pozanenko A., Chelovekov I., Grebenev S., GRB IKI FuN, 2021, GRB Coordinates Network, 30444, 1
- Mukai K., 1993, *Legacy*, 3, 21
- Mullis C. R. et al., 2003, *ApJ*, 594, 154
- Nakar E., Piran T., Granot J., 2003, *New Astron.*, 8, 495
- Narayana Bhat P. et al., 2016, *ApJS*, 223, 28
- Norris J. P., Bonnell J. T., 2006, *ApJ*, 643, 266
- Norris J. P., Cline T. L., Desai U. D., Teegarden B. J., 1984, *Nature*, 308, 434
- Nugent A. E. et al., 2022, *ApJ*, 940, 57
- O’Connor B. et al., 2022, *MNRAS*, 515, 4890
- Palmerio J. T. et al., 2019, *A&A*, 623, A26
- Pankov N., Belkin S., Kim V., Pozanenko A., Krugov M., GRB IKI FuN, 2021, GRB Coordinates Network, 30440, 1
- Patat F. et al., 2001, *ApJ*, 555, 900
- Pereyra M. et al., 2022, *MNRAS*, 511, 6205
- Perley D. A. et al., 2013, *ApJ*, 778, 128
- Perley D. A. et al., 2020, *ApJ*, 904, 35
- Piro A. L., Haynie A., Yao Y., 2021, *ApJ*, 909, 209
- Planck Collaboration VI, 2020, *A&A*, 641, A6
- Pogge R. W. et al., 2010, in McLean I. S., Ramsay S. K., Takami H. eds, Proc. SPIE Conf. Ser. Vol. 7735, Ground-based and Airborne Instrumentation for Astronomy III. SPIE, Bellingham, p. 77350A
- Prasad V. et al., 2021, GRB Coordinates Network, 30378, 1
- Prentice S. J. et al., 2018, *ApJ*, 865, L3

- Pursiainen M. et al., 2025, *MNRAS*, 537, 3298
- Quirola-Vásquez J. et al., 2026, *MNRAS*, 545, staf2064
- Rastinejad J. C. et al., 2022, *Nature*, 612, 223
- Rastinejad J. C. et al., 2025, *ApJ*, 988, L13
- Rees M. J., Mészáros P., 1998, *ApJ*, 496, L1
- Ridnaia A. et al., 2021, GRB Coordinates Network, 30388, 1
- Roming P. W. A. et al., 2005, *Space Sci. Rev.*, 120, 95
- Rossi A. et al., 2022, *ApJ*, 932, 1
- Rosswog S., 2007, *MNRAS*, 376, L48
- Ryan G., van Eerten H., Piro L., Troja E., 2020, *ApJ*, 896, 166
- SDSS Collaboration, 2025, preprint ([arXiv:2507.07093](https://arxiv.org/abs/2507.07093))
- Sari R., Mészáros P., 2000, *ApJ*, 535, L33
- Sarin N., Omand C. M. B., Margalit B., Jones D. I., 2022, *MNRAS*, 516, 4949
- Sarin N. et al., 2024, *MNRAS*, 531, 1203
- Sarin N. et al. 2025 Zenodo
- Schlafly E. F., Finkbeiner D. P., 2011, *ApJ*, 737, 103
- Shu X. et al., 2025, *ApJ*, 990, L29
- Skrutskie M. F. et al., 2006, *AJ*, 131, 1163
- Srivastav S. et al., 2025, *ApJ*, 978, L21
- Stratta G. et al., 2025, *ApJ*, 979, 159
- Sun H. et al., 2025, *Nat. Astron.*, 9, 1073
- Sun T. R., Hu Y. D., Fernández-García E., Castro-Tirado A. J., Caballero-García M. D., Castro Tirado M. A., Martín-Fernández P., 2021, GRB Coordinates Network, 30411, 1
- Sun T.-R. et al., 2024, *ApJ*, 976, L20
- Talbot C. et al., 2025, Zenodo
- Tam P. H., Pun C. S. J., Huang Y. F., Cheng K. S., 2005, *New Astron.*, 10, 535
- Tanaka M., Ikeda H., Murata K., Takita S., Mineo S., Koike M., Okura Y., Harasawa S., 2021, *PASJ*, 73, 735
- Tanvir N. R., Levan A. J., Fruchter A. S., Hjorth J., Hounsell R. A., Wiersema K., Tunnicliffe R. L., 2013, *Nature*, 500, 547
- The Matplotlib Development Team, 2025, Zenodo
- The Pandas Development Team, 2025, Zenodo
- Tody D., 1986, in Crawford D. L. ed., *Proc. SPIE Conf. Ser. Vol. 627, Instrumentation in Astronomy VI*. SPIE, Bellingham, p. 733
- Tody D., 1993, in Hanisch R. J., Brissenden R. J. V., Barnes J. eds, ASP Conf. Ser. Vol. 52, *Astronomical Data Analysis Software and Systems II*. Astron. Soc. Pac., San Francisco, p. 173
- Troja E. et al., 2022, *Nature*, 612, 228
- Ursi A. et al., 2021, GRB Coordinates Network, 30372, 1
- Van Dalen J. N. D. et al., 2025, *ApJ*, 982, L47
- van Eerten H., 2018, *Int. J. Mod. Phys. D*, 27, 1842002
- van Eerten H., Zhang W., MacFadyen A., 2010, *ApJ*, 722, 235
- Villar V. A. et al., 2017, *ApJ*, 851, L21
- Volnova A., Moskvitin A., Pozanenko A., Pankov N., Belkin S., GRB IKI FuN, 2021, GRB Coordinates Network, 30465, 1
- Von Kienlin A. et al., 2014, *ApJS*, 211, 13
- Von Kienlin A. et al., 2020, *ApJ*, 893, 46
- Wallace W. F., Sarin N., 2025, *MNRAS*, 539, 3319
- Wang X., Loeb A., 2000, *ApJ*, 535, 788
- Watson A. M. et al., 2021, GRB Coordinates Network, 30436, 1
- Whitesides L. et al., 2017, *ApJ*, 851, 107
- Williams M. J., Veitch J., Messenger C., 2021, *Phys. Rev. D*, 103, 103006
- Williams M. J., Veitch J., Messenger C., 2023, *Machine Learn. Sci. Technol.*, 4, 035011
- Williams M. J., Veitch J., Chapman-Bird C., 2025, Zenodo
- Woolsey S. E., Sukhbold T., Kasen D. N., 2021, *ApJ*, 913, 145
- Wu G.-L. et al., 2025, *ApJ*, 991, 115
- Yadav M. et al. 2025, *ApJ*, 995, 216
- Yang B. et al., 2015, *Nat. Commun.*, 6, 7323
- Yang J. et al., 2022, *Nature*, 612, 232
- Yang Y.-H. et al., 2024, *Nature*, 626, 742
- Zhang B., Mészáros P., 2002, *ApJ*, 566, 712
- Zhang B., Yan H., 2011, *ApJ*, 726, 90
- Zhang B., Fan Y. Z., Dyks J., Kobayashi S., Mészáros P., Burrows D. N., Nousek J. A., Gehrels N., 2006, *ApJ*, 642, 354

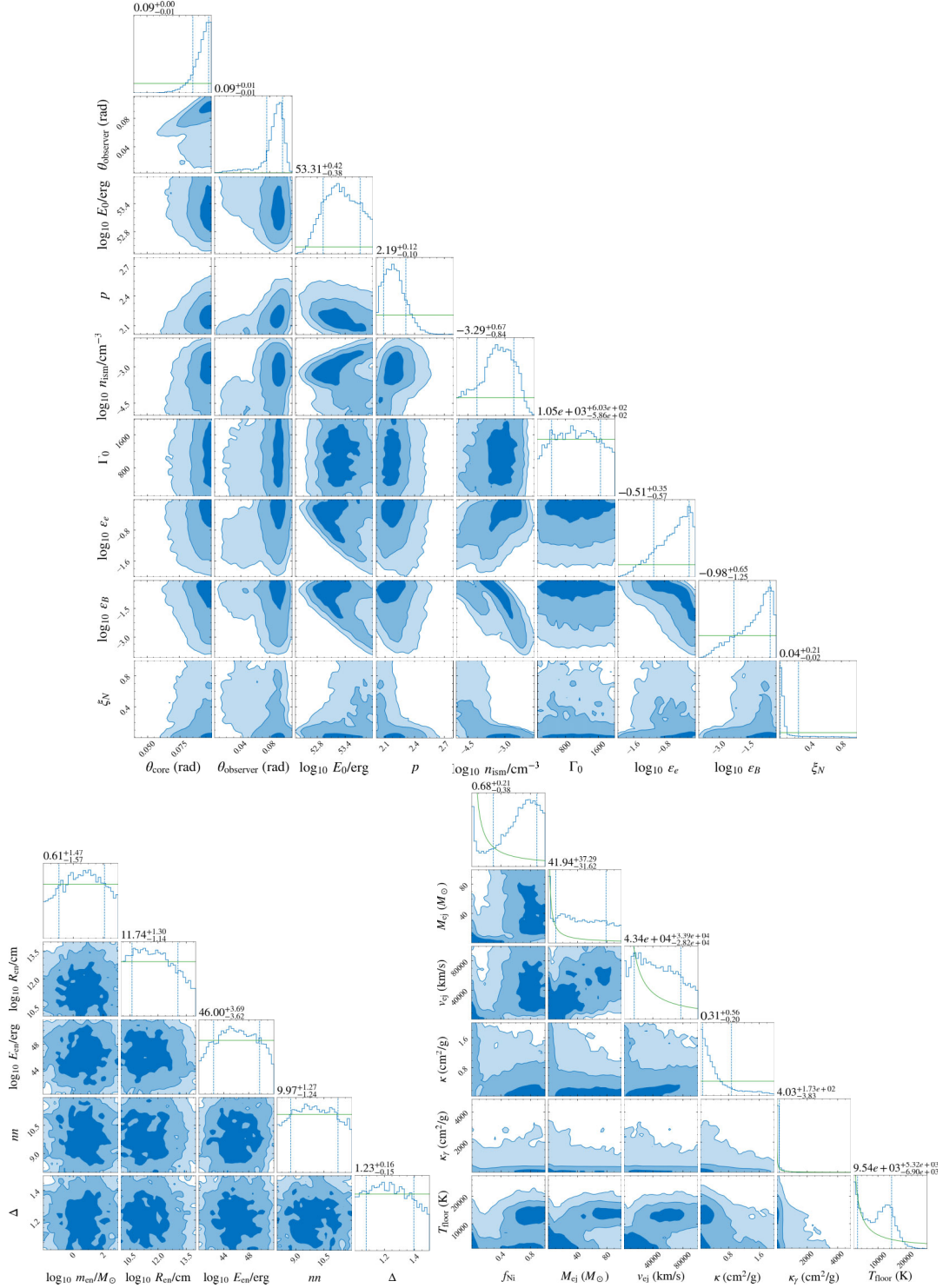
## APPENDIX A: CORNER PLOTS



**Figure A1.** Posterior distribution from the joint fit using a top-hat afterglow model (upper plot; G. Ryan et al. 2020), an SN-CSM interaction model (lower left plot; B. Margalit 2022), and an SN model (lower right plot; W. D. Arnett 1982). The graphs in the histogram panels correspond to the prior distributions. The parameter values above the histograms are the median, where the 16th and 84th percentiles represent the error bars (also indicated by the vertical dashed lines in the histograms). The posterior parameters for the top-hat model are the jet opening angle  $\theta_{\text{core}}$ , viewing angle  $\theta_{\text{observer}}$ , jet energy  $E_0$ , electron power-law index  $p$ , CSM number density  $n_{\text{ism}}$ , initial Lorentz factor  $\Gamma_0$ , partition fractions in electrons ( $\epsilon_e$ ) and in magnetic field ( $\epsilon_B$ ), and the fraction of electrons that get accelerated  $\xi_N$ . For the CSM interaction model, the parameters are the CSM-shell mass  $M_{\text{CSM}}$ , minimum ejecta velocity  $v_{\text{ej}}$ , velocity ratio  $\beta = v/c$ , effective opacity  $\kappa$ , and the radius and width of the shell ( $R_{\text{shell}}$  and  $\Delta R_{\text{shell}}$ ). For the SN model, the parameters are the nickel mass fraction  $f_{\text{Ni}}$ , total ejecta mass  $M_{\text{ej}}$ , opacity to gamma-rays  $\kappa_{\gamma}$ , temperature floor  $T_{\text{floor}}$ , and  $v_{\text{ej}}$  and  $\kappa$  that are also in the CSM interaction model.



**Figure A2.** Posterior distribution from the joint fit using a refreshed top-hat afterglow model (upper left plot for the standard afterglow parameters and upper right plot for the refreshed shock parameters; G. P. Lamb et al. 2019; G. P. Lamb et al. 2020) and an SN model (lower plot; W. D. Arnett 1982). The graphs in the histogram panels correspond to the prior distributions. The parameter values above the histograms are the median, where the 16th and 84th percentiles represent the error bars (also indicated by the vertical dashed lines in the histograms). The posterior parameters for the top-hat model are the jet opening angle  $\theta_{\text{core}}$ , viewing angle  $\theta_{\text{observer}}$ , jet energy  $E_0$ , electron power-law index  $p$ , CSM number density  $n_{\text{ism}}$ , initial Lorentz factor  $\Gamma_0$ , partition fractions in electrons ( $\epsilon_e$ ) and in magnetic field ( $\epsilon_B$ ), and the fraction of electrons that get accelerated  $\xi_N$ . For the refreshed shock, the parameters are the Lorentz factor of the shell at the start of energy injection  $\Gamma_1$ , the factor by which the kinetic energy is larger  $E_t$ , and the index of energy injection  $s_1$ . For the SN model, the parameters are the nickel mass fraction  $f_{\text{Ni}}$ , total ejecta mass  $M_{\text{ej}}$ , minimum ejecta velocity  $v_{\text{ej}}$ , effective opacity  $\kappa$ , opacity to gamma-rays  $\kappa_{\gamma}$ , and the temperature floor  $T_{\text{floor}}$ .



**Figure A3.** Posterior distribution from the joint fit using a top-hat afterglow model (upper plot; G. Ryan et al. 2020), shock cooling model (lower left plot; A. L. Piro et al. 2021) and an SN model (lower right plot; W. D. Arnett 1982). The graphs in the histogram panels correspond to the prior distributions. The parameter values above the histograms are the median, where the 16th and 84th percentiles represent the error bars (also indicated by the vertical dashed lines in the histograms). The posterior parameters for the top-hat model are the jet opening angle  $\theta_{\text{core}}$ , viewing angle  $\theta_{\text{observer}}$ , jet energy  $E_0$ , electron power-law index  $p$ , CSM number density  $n_{\text{ism}}$ , initial Lorentz factor  $\Gamma_0$ , partition fractions in electrons ( $\epsilon_e$ ) and in magnetic field ( $\epsilon_B$ ), and the fraction of electrons that get accelerated  $\xi_N$ . For the shock cooling model, the parameters are the mass  $m_{\text{en}}$ , energy  $E_{\text{en}}$ , and radius  $R_{\text{en}}$  of the extended material and the power-law density slopes of the outer and inner extended material components ( $nn$  and  $\Delta$ , respectively). For the SN model, the parameters are the nickel mass fraction  $f_{\text{Ni}}$ , total ejecta mass  $M_{\text{ej}}$ , minimum ejecta velocity  $v_{\text{ej}}$ , effective opacity  $\kappa$ , opacity to gamma-rays  $\kappa_{\gamma}$ , and the temperature floor  $T_{\text{floor}}$ .

<sup>1</sup>*Department of Astrophysics/IMAPP, Radboud University Nijmegen, P.O. Box 9010, NL-6500 GL Nijmegen, the Netherlands*

<sup>2</sup>*Department of Physics, University of Warwick, Coventry CV4 7AL, UK*

<sup>3</sup>*INAF – Osservatorio Astronomico di Brera, Via E. Bianchi 46, I-23807 Merate, Italy*

<sup>4</sup>*Center for Interdisciplinary Exploration and Research in Astrophysics (CIERA) and Department of Physics and Astronomy, Northwestern University, Evanston, IL 60208, USA*

<sup>5</sup>*Department of Astronomy, University of Maryland, College Park, MD 20742, USA*

<sup>6</sup>*Cosmic Dawn Center (DAWN), Denmark*

<sup>7</sup>*Niels Bohr Institute, University of Copenhagen, Jagtvej 155, DK-2200 Copenhagen N, Denmark*

<sup>8</sup>*Kavli Institute for Cosmology Cambridge, Madingley Road, Cambridge CB3 0HA, UK*

<sup>9</sup>*Institute of Astronomy, University of Cambridge, Madingley Road, Cambridge CB3 0HA, UK*

<sup>10</sup>*Astrophysics Research Institute, Liverpool John Moores University, IC2 Liverpool Science Park, 146 Brownlow Hill, Liverpool L3 5RF, UK*

<sup>11</sup>*School of Physics and Centre for Space Research, O'Brien Centre for Science North, University College Dublin, Belfield, Dublin 4, Ireland*

<sup>12</sup>*Center for Astrophysics|Harvard & Smithsonian, 60 Garden Street, Cambridge, MA 02138, USA*

<sup>13</sup>*School of Physics and Astronomy, University of Leicester, University Road, Leicester LE1 7RH, UK*

<sup>14</sup>*Hessian Research Cluster ELEMENTS, Giersch Science Center, Max-von-Laue-Strasse 12, Goethe University Frankfurt, Campus Riedberg, D-60438 Frankfurt am Main, Germany*

<sup>15</sup>*Instituto de Astrofísica de Andalucía (IAA-CSIC), Glorieta de la Astronomía s/n, E-18008 Granada, Spain*

<sup>16</sup>*Centro Astronómico Hispano en Andalucía, Observatorio de Calar Alto, Sierra de los Filabres, E-04550 Gérgal, Almería, Spain*

<sup>17</sup>*INAF – Osservatorio di Astrofisica e Scienza dello Spazio, Via Piero Gobetti 93/3, I-40024 Bologna, Italy*

<sup>18</sup>*Space Science Data Center (SSDC) – Agenzia Spaziale Italiana (ASI), I-00133 Roma, Italy*

<sup>19</sup>*Aix Marseille University, CNRS, CNES, LAM, Marseille, France*

<sup>20</sup>*School of Physics and Astronomy, University of Birmingham, Edgbaston, Birmingham B15 2TT, UK*

<sup>21</sup>*Institute for Gravitational Wave Astronomy, University of Birmingham, Birmingham B15 2TT, UK*

<sup>22</sup>*INAF – Osservatorio Astronomico di Capodimonte, Salita Moiariello 16, I-80131 Naples, Italy*

<sup>23</sup>*DARK, Niels Bohr Institute, University of Copenhagen, Jagtvej 128, DK-2200 Copenhagen, Denmark*

<sup>24</sup>*INAF – Osservatorio Astronomico di Roma, Via di Frascati 33, I-00040 Monte Porzio Catone (RM), Italy*

<sup>25</sup>*European Space Agency (ESA), European Space Astronomy Centre (ESAC), Camino Bajo del Castillo s/n, E-28692 Villanueva de la Cañada, Madrid, Spain*

This paper has been typeset from a  $\text{\TeX}/\text{\LaTeX}$  file prepared by the author.